ELSEVIER

Physica D 143 (2000) 21–55

PHYSICA D

www.elsevier.com/locate/physd

A shocking display of synchrony

Neil J. Balmforth [a,*], Roberto Sassi [b]

[a] *Department of Applied Mathematics and Statistics, University of California, Santa Cruz, CA 95064, USA*
[b] *Dipartimento di Bioingegneria, Politecnico di Milano, Piazza Leonardo da Vinci 32, 20133 Milan, Italy*

Abstract

This article explores the Kuramoto model describing the synchronization of a population of coupled oscillators. Two versions of this model are considered: a discrete version suitable for a population with a finite number of oscillators, and a continuum model found in the limit of an infinite population. When the strength of the coupling between the oscillators exceeds a threshold, the oscillators partially synchronize. We explore the transition in the continuum model, which takes the form of a bifurcation of a discrete mode from a continuous spectrum. We use numerical methods and perturbation theory to study the patterns of synchronization that form beyond transition, and compare with the synchronization predicted by the discrete model. There are similarities with instabilities in ideal plasmas and inviscid fluids, but these are superficial. © 2000 Published by Elsevier Science B.V.

PACS: 05.45.Xt; 05.45.−a; 87.10.+e

Keywords: Coupled oscillators; Bifurcations; Synchronization

1. Introduction

Mutual synchronization is a common phenomenon in biology. It occurs at different levels in and among many different organisms. For example, synchronization occurs on a small-scale of the cardiac pace-maker cells of the SA (sinoatrial) and AV (atrioventricular) nodes in the human hearth that synchronously fire and give the pace to the whole muscle. But synchrony also arises as the coordinated behaviours of crickets that chirp in unison and of fireflies that flash together. Although this article is motivated by these biological problems, our aim here is primarily mathematical and not directly relevant to biology; we study an idealized mathematical model constructed to explore the dynamics of a population of coupled oscillators.

In the biological context, mathematical studies of problems of this kind began with van der Pol's analogy between the heart and a system of coupled relaxation oscillators, and with Wiener's interpretation of the alpha rhythms in the human brain in terms of synchronously firing neurons. Somewhat later, Winfree [1] highlighted the generality of the synchronization problem, and fixed some simple first assumptions for a mathematical model. Subsequently, Kuramoto [2] built on Winfree's ideas and proposed a detailed model in which each oscillator is identical to the

* Corresponding author.
E-mail address: njb@cse.ucsc.edu (N.J. Balmforth)

0167-2789/00/$ – see front matter © 2000 Published by Elsevier Science B.V.
PII: S0167-2789(00)00095-6

others upto the frequency and phase (so that the amplitudes are all constant and equal), and the ensemble is coupled through a *mean field*. The equation of the model for the nth oscillator is

$$\frac{\mathrm{d}\theta_n}{\mathrm{d}t} = \omega_n + \frac{K}{N}\sum_{j=1}^{N} f(\theta_j - \theta_n) + \xi_n, \tag{1}$$

where ω_n is a random variable chosen from a distribution with a probability density function $g(\omega)$, K is the *coupling strength*, $f(\phi)$ is the form of coupling and ξ_n is white noise. Kuramoto, and most subsequent workers, have further set $f(\phi) = \sin\phi$. We, too, will follow that lead and use this mean field throughout the current article (but see [3,4] and our final remarks).

Because the model is composed of distinct oscillators, we refer to the set (1) of ordinary differential equations (ODEs) as the discrete Kuramoto model. [1] This system is not just an idealized mathematical toy that describes biological populations but has also appeared as a normal-form equation for systems of general coupled oscillators; for example, the model arises as an asymptotic description of a weakly coupled or disordered array of Josephson junctions [5].

Following Kuramoto, we define an *order parameter*, r, through the relation

$$r\mathrm{e}^{\mathrm{i}\psi} = \frac{1}{N}\sum_{j=1}^{N}\mathrm{e}^{\mathrm{i}\theta_j}. \tag{2}$$

This parameter measures the synchronization among the oscillator phases: $r = 0$ corresponds to the completely incoherent state, and finite r to some level of synchrony. The information contained in the phase, ψ, is mostly ignored.

Kuramoto studied steadily oscillating populations in the case of no added random noise ($\xi_n = 0$), and showed that the incoherent state $r = 0$ exists for all coupling strengths. More interestingly, he also showed that there were other, non-trivial solutions with a finite degree of synchrony in the population. Specifically, these are populations for which the oscillator frequencies become modified to

$$\hat{\omega}_n = \begin{cases} \Omega & \text{for } |\omega_n - \Omega| < Kr, \\ \Omega + (\omega_n - \Omega)\sqrt{1 - K^2r^2/(\omega_n - \Omega)^2} & \text{for } |\omega_n - \Omega| > Kr, \end{cases} \tag{3}$$

where Ω is the frequency of the synchronized sub-population. Kuramoto found that these partly synchronized populations exist for coupling strengths that exceed some critical threshold: $K > K_\mathrm{c} = 2/[\pi g(0)]$. Below that threshold, only incoherent populations exist. In a particular case with a Lorentzian frequency distribution, $g(\omega) = [\pi(1+\omega^2)]^{-1}$, Kuramoto derived the relation

$$r = \sqrt{1 - 2/K} \tag{4}$$

(and $\Omega = 0$) for the partly synchronized populations, the critical threshold being $K_\mathrm{c} = 2$. Eq. (4) illustrates a near-threshold scaling behaviour, $r \sim (K - K_\mathrm{c})^\beta$ with $\beta = \frac{1}{2}$, which also holds for general $g(\omega)$ [6].

The synchronized sub-populations are apparently stable in the discrete model, and so their appearance coincides with the onset of order, as in a phase transition. When noise is added to the system, a similar threshold and transition arises, although the value of the critical coupling strength, K_c, is different. To illustrate the dynamics, we display the results of numerical simulations of the ODEs (1), with $N = 256$ and two different values of the coupling parameter K in Fig. 1; we add noise in the form of random perturbations ξ_n drawn from a normal distribution with

[1] By "discrete" here we refer to a finite population; later we use "continuous" to mean the infinite population. This terminology should be distinguished from other models in which one uses a discrete time variable (so the governing equations are coupled maps rather than ODEs).

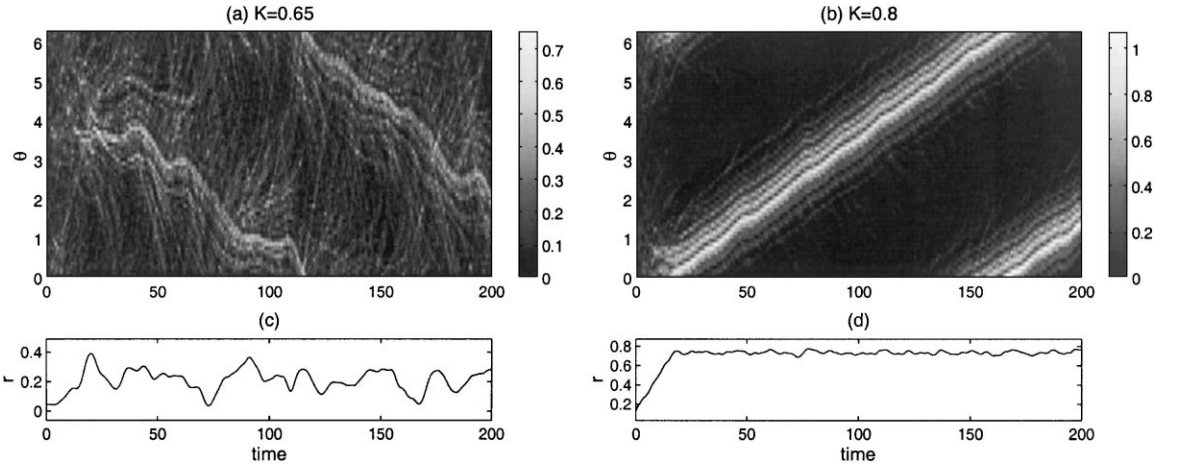

Fig. 1. Numerical simulations of the discrete Kuramoto model with $N = 256$ and $D = 0.01$. The frequencies are selected from the distribution (24), and the initial condition is a population of oscillators with phases chosen in $[0, 2\pi]$ according to the distribution described in Section 4 with $a = 2$, $\xi = 0.1$ and $L = 0$. Panels (a) and (c) show a sub-threshold case with $K = 0.65 \approx 0.9K_c$, and panels (b) and (d) show an unstable case with $K = 0.80 \approx 1.1K_c$ ($K_c = 0.739$). Panels (a) and (b) show time evolution of the probability density function computed by counting the number of oscillators whose instantaneous values of θ_n fall into bins of size $\pi/32$; the density in the bins is then shaded according to the greyscale displayed in the key. Panels (c) and (d) show the time evolution of the order parameter, r.

standard deviation $2D = 0.02$. In the upper panels of these figures, we show the time evolution of the instantaneous distribution of phases of the oscillators, obtained by dividing the interval of θ into a finite number of bins (in this case 64) and counting the number of oscillators in each bin. In the lower panels, the time evolution of the order parameter, r, is displayed.

For the case shown on the left, the coupling strength is below threshold: $K = 0.65 < K_c$. Here, the order parameter fluctuates at low amplitude, indicating that a collective, coherent behaviour does not suddenly appear. In the phase distribution, however, some low-amplitude collective structures can be noticed: a small population of oscillators cluster in phase and drift erratically. Presumably this structure is connected to the vacillations in r, but there is no tendency for strong, sustained synchrony. By contrast, when $K = 0.8 > K_c$, in a very short time the phases of the oscillators gather together in a small range of angles and then drift coherently. The amplitude of the order parameter grows quickly, and then saturates, whereupon it exhibits small fluctuations. In other words, a fraction of the population synchronizes.

The discrete model formulated by Kuramoto has the advantage that it is straightforward to solve numerically for a small number of oscillators, but the procedure becomes unweildy once the population becomes large. Moreover, the discrete formulation is not especially suited to analytical avenues of approach. An alternative approach is to take the continuum limit of the discrete model [7,8] and capture the behaviour of an infinite population, $N \to \infty$. The continuous model takes the form of a partial differential equation (PDE) for the distribution, $\rho(\theta, \omega, t)$, of the oscillators in phase and frequency at time t. In this study, we adopt this model, and explore the predicted dynamics of the oscillator population. In particular, we study in detail the dynamics in the vicinity of the critical coupling threshold K_c.

In the PDE, the transition occurs when the incoherent equilibrium state, $\rho = (2\pi)^{-1}$, suffers the onset of a linear instability. The instability takes the form of a normal mode with structure in θ; when this mode grows to finite amplitude and saturates nonlinearly, a synchronized state appears. This rationalizes Kuramoto's transition in terms of bifurcation theory.

Several previous works [9,10] have also studied this transition, dealing mainly with the noisy version of the formulation. In the continuum description, the noise is modelled by a diffusion in angle θ. Consequently, the PDE is dissipative and techniques of centre-manifold reduction furnish a simple amplitude equation for the onset of θ-structured states (see Section 8.1). Here we are more interested in the limit in which the noise is very slight, and to leading order, the PDE is non-dissipative. This is the case considered by Crawford and Davies [3] and that article played a key role in motivating the present study.

The important facet of the non-dissipative problem that changes the complexion of the transition is the linear eigenvalue spectrum of the incoherent state. Unlike many dissipative systems, that eigenspectrum contains a neutrally stable continuous spectrum. Moreover, although the instability results from a discrete normal mode, the distinguished mode bifurcates to instability by detaching from the continuous spectrum. This added ingredient to the problem leads to significant complications in the weakly nonlinear description. Notably, because at onset there is no separation between the distinguished mode and the remainder of the spectrum, we cannot apply centre-manifold techniques directly, and standard weakly nonlinear expansion fails (but see [3]).

Similar difficulties arise for ideal plasmas [11,12] and inviscid shear flows [13–16]. In these situations, the unstable mode is also embedded in a continuous spectrum at the onset of instability. The failure of standard weakly nonlinear techniques is seen as the appearance of singularities in the equations along a special surface that locates the wave-particle resonance for the plasma, and the inviscid critical level for the fluid. To circumvent the singularities, one abandons the standard weakly nonlinear theory in a slender region surrounding the singular level. In this *critical layer* one finds another solution that varies on a much finer spatial scale, and then matches with the customary weakly nonlinear solution which remains valid outside. In other words, one proceeds with a matched asymptotic expansion. But the essential physical point is that the mode, as it grows, overturns the plasma or fluid inside the critical layer and generates a "cat's eye" pattern. This physical effect is not captured in the relatively simple structure of the unstable mode, and a low-order equation for the modal amplitude is unable to describe the dynamics of the forming patterns. By performing matched asymptotics, we add the needed extra physics. One of our goals in this article is to explore the parallel for synchronizing populations of coupled oscillators.

The similarity in the linear problem also poses further questions in the coupled oscillator problem. For example, pattern formation can result even for stable fluid flows or plasma equilibria; do oscillator populations also show such sub-threshold effects? Less specifically, the fact that all three problems are characterized by a bifurcation from the continuous spectrum leads one to wonder whether there is some underlying, unifying "normal form" that may guide theoretical explorations. In this article, we also consider the Kuramoto model in this light.

2. Mathematical formulation

2.1. The continuous model

The continuous version of the model takes the form of a PDE for the distribution, $\rho(\theta, \omega, t)$, of the oscillators in phase and frequency at time t:

$$\rho_t + \omega\rho_\theta + K(\rho G)_\theta = D\rho_{\theta\theta}, \tag{5}$$

where

$$G(\theta, t) = \int_{-\infty}^{\infty}\int_0^{2\pi} f(\phi - \theta)\rho(\phi, \omega, t)g(\omega)\,\mathrm{d}\phi\,\mathrm{d}\omega, \tag{6}$$

$\theta \in [0; 2\pi]$ and $\omega \in [-\infty; \infty]$, and as described in Section 1, we take $f(\theta) = \sin\theta$ until Section 11. The density function ρ is periodic in θ and must also satisfy, for each ω, a normalization law

$$\int_0^{2\pi} \rho(\theta, \omega, t)\, \mathrm{d}\theta = 1. \tag{7}$$

The derivation of these equations has the flavour of the BBGKY hierarchy in plasma physics and can be found in [3].

The system has equilibrium solutions with ρ independent of θ, which represent incoherent states. For these states, any structure in ω reflects an internal frequency distribution. But this frequency structure supplements the intrinsic frequency variation of the uncoupled oscillators given by $g(\omega)$, and is therefore superfluous. The only equilibrium state of relevance is the particular solution, $\rho = (2\pi)^{-1}$, for which the oscillators are uniformly distributed in frequency, but their intrinsic frequencies are distributed according to $g(\omega)$.

Our measure of order in (2) becomes, in the continuous limit

$$r\mathrm{e}^{\mathrm{i}\psi} = \int_{-\infty}^{\infty}\int_0^{2\pi} \mathrm{e}^{\mathrm{i}\theta}\rho(\theta, \omega, t)g(\omega)\, \mathrm{d}\theta\, \mathrm{d}\omega. \tag{8}$$

Strictly speaking, when $f(\theta) \neq \sin\theta$, this definition should be generalized [4].

2.2. Symmetrical systems

The equations are symmetrical under the transformation, $\rho(\theta, \omega, t) = \rho(-\theta, -\omega, t)$, provided $g(\omega)$ is an even function and the initial condition also possesses the symmetry. We refer to populations with this property as symmetrical systems. The symmetry has the useful consequence that $G(\theta, t)$ is separable in θ and t:

$$G(\theta, t) = -\mathcal{G}(t)\sin\theta, \tag{9}$$

where

$$\mathcal{G}(t) = \int_{-\infty}^{\infty}\int_0^{2\pi} \rho(\theta, \omega, t)g(\omega)\cos\theta\, \mathrm{d}\theta\, \mathrm{d}\omega, \tag{10}$$

$$\int_{-\infty}^{\infty}\int_0^{2\pi} \rho(\theta, \omega, t)g(\omega)\sin\theta\, \mathrm{d}\theta\, \mathrm{d}\omega = 0. \tag{11}$$

Moreover, $r\mathrm{e}^{\mathrm{i}\psi} \to \mathcal{G}(t)$, and so $\psi = 0$ or π, and $r \equiv |\mathcal{G}(t)|$. In later sections we exploit this symmetry.

3. Linear theory

We commence our study of the Kuramoto model by discussing the linear stability of the incoherent state, $\rho = (2\pi)^{-1}$. To some degree, this repeats the work of Strogatz and Mirollo [8], but we sketch results which prove useful for the discussion that follows.

We perturb ρ around the steady-state solution:

$$\rho = \frac{1}{2\pi} + \sum_{m=0}^{\infty}[c_m(\omega, t)\mathrm{e}^{\mathrm{i}m\theta} + \text{c.c.}], \tag{12}$$

where c.c. denotes complex conjugate and m is the integral angular wave number. With this decomposition, we find

$$G \equiv \mathrm{i}\pi \mathrm{e}^{\mathrm{i}\theta} \int_{-\infty}^{\infty} c_1(\omega, t) g(\omega)\, \mathrm{d}\omega + \text{c.c.} \quad \text{or} \quad \mathcal{G}(t) = 2\pi \int_{-\infty}^{\infty} c_1(\omega, t) g(\omega)\, \mathrm{d}\omega, \tag{13}$$

and a linearization of Eq. (5) gives

$$c_{mt} = -(m^2 D + \mathrm{i}m\omega) c_m + \frac{1}{2} K \delta_{m1} \int_{-\infty}^{\infty} c_m(\nu, t) g(\nu)\, \mathrm{d}\nu \tag{14}$$

3.1. Eigenvalue spectrum

The eigenvalue spectrum can be computed by seeking solutions with temporal dependence, $\mathrm{e}^{\lambda t}$. Also, because of the form of the coupling function $f(\phi) = \sin\phi$, only the $m = 1$ mode appears in the mean field and is therefore important to stability. For this mode, it is straightforward to derive

$$\mathcal{D}(\lambda) \equiv 1 - \frac{1}{2} K \int_{-\infty}^{\infty} \frac{g(\omega)}{\lambda + D + \mathrm{i}\omega}\, \mathrm{d}\omega = 0. \tag{15}$$

There is a discrete eigenvalue provided $\mathcal{D}(\lambda)$ has a zero somewhere in the spectral (complex λ) plane. When $\mathrm{Re}(\lambda) < 0$, the discrete mode is damped and its contribution to an arbitrary initial perturbation will decay with time. If $\mathrm{Re}(\lambda) > 0$, on the other hand, the discrete mode is unstable.

However, the eigenvalue problem is not as straightforward as it first seems: the dispersion function $\mathcal{D}(\lambda)$ has the form of a Cauchy integral and is not an analytic function over the whole complex λ-plane. The non-analyticity reflects the presence of the continuous spectrum along the line $\lambda = -D - \mathrm{i}\omega$ (see [8]).

By way of illustration, consider a delta-function and a Lorentzian frequency distribution:

$$g_1(\omega) = \delta(\omega) \quad \text{and} \quad g_2(\omega) = [\pi(1 + \omega^2)]^{-1}. \tag{16}$$

In these cases we may explicitly perform the integral in the dispersion relation. Then

$$\lambda = -D + \tfrac{1}{2}K \quad \text{and} \quad \lambda = -D + \tfrac{1}{2}K - \mathrm{sgn}(\lambda + D). \tag{17}$$

The second of these expressions is non-analytic for $\lambda = -D$, as expected. The relation for the delta-function frequency, however, is analytic, which illustrates how this particular frequency distribution is special because the continuous spectrum decouples from the discrete mode. The mode is unstable for $K > K_\mathrm{c}$, with

$$K_\mathrm{c} = 2D \quad \text{and} \quad K_\mathrm{c} = 2 + 2D. \tag{18}$$

This is the critical coupling strength.

For the Lorentzian, we summarize the stability calculation as follows: For $0 < K \leq 2$, the system is stable and has no discrete modes. At $K = 2$, an eigenmode appears out of the continuous spectrum, and when $2 < K < 2+2D$ the system has a single discrete mode, but is still stable. If $K > 2 + 2D$ there is an unstable growing mode. If the dissipation is zero, the system can only be either unstable, with a growing mode ($K > 2$), or neutrally stable with no discrete modes ($K \leq 2$). Moreover, the eigenmode bifurcates out of the continuous spectrum at the onset of instability.

3.2. An initial-value problem

Although the incoherent state is only neutrally stable when $D = 0$ and $K < K_\mathrm{c}$, the order parameter still decays with time in the linear initial-value problem. The decay reflects the phase mixing of integral superpositions of modes in the continuous spectrum and as pointed out by Strogatz et al. [17], is analogous to Landau damping in plasmas.

We illustrate this peculiar form of damping by solving the initial value problem for the Lorentzian frequency distribution with $K < K_c$, $D = 0$ and the initial condition

$$c_1(\omega, 0) = \frac{a}{\pi}\frac{e^{iL\omega}}{\omega^2 + a^2} + \text{c.c.}, \tag{19}$$

where $L \geq 0$ and a are constants. By using Laplace transforms, we may derive the solution

$$\begin{aligned}\mathcal{G} = {} & \frac{2aK}{(a^2-1)}\left[\frac{e^{-L}}{K-4} - \frac{e^{-aL}}{a(K-2a-2)}\right]e^{(K/2-1)t} \\ & +4\left[\frac{2ae^{t-L}}{(a^2-1)(4-K)} - \frac{e^{a(t-L)}}{(a-1)(2a+2-K)}\right]H(L-t) \\ & +4\left[\frac{8ae^{(K-2)(t-L)}}{[(K-2)^2-4a^2](K-4)} + \frac{e^{-a(t-L)}}{(a+1)(2-2a-K)}\right]H(t-L),\end{aligned} \tag{20}$$

where $H(t)$ is the Heaviside function.

To highlight the Landau damping, we take $L = 0$. Then

$$\mathcal{G} = \frac{2(K+2a)e^{(K/2-1)t} - 4e^{-at}}{(a+1)(K+2a-2)}. \tag{21}$$

Evidently, the order parameter decays exponentially for $K < 2$. Part of this decay, given by the term proportional to $e^{(K/2-1)t}$, reflects an intrinsic property of the oscillator population, and its form is not dependent on the initial condition (except for the numerical value of the prefactor); this is Landau damping. The other decaying term in (21) is not a general property of the population and arises from the form of the initial condition (as evidenced by the damping rate, which depends on the width of the Lorentzian initial condition); this second form of damping is usually ignored in comparison to Landau damping, often without justification. We refer to the combined effect as *continuum damping*, and is illustrated in Fig. 2. This figure shows the order parameter for this particular case, and two other cases with $L \neq 0$.

For general L, in addition to the ultimate decay, Eq. (20) also indicates that there can be sustained transients: for $t < L$, the order parameter contains exponentially growing terms (see Fig. 2 for $L = 20$ and 40). We discuss the transients in more detail a little later. But all of these features of the linear, initial-value problem are familiar from plasma theory and fluid dynamics [18,19]. Soon, we answer the question of whether the nonlinear dynamics is also similar.

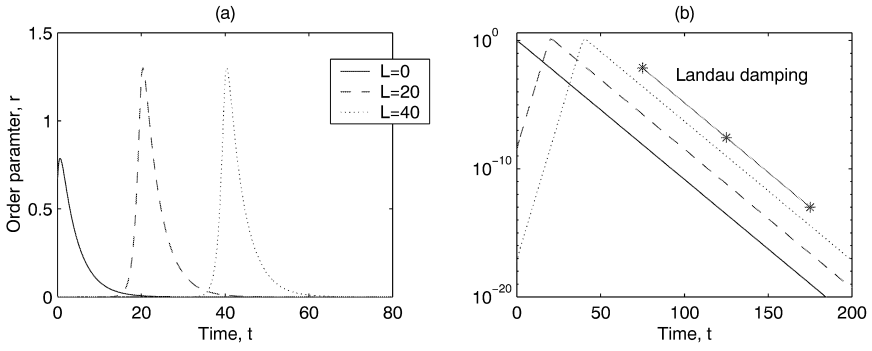

Fig. 2. Evolution of the order parameter for $K = 1.5$, $a = 2$ and three values of L (0, 20 and 40). In the second panel, the trend of Landau damping is also shown.

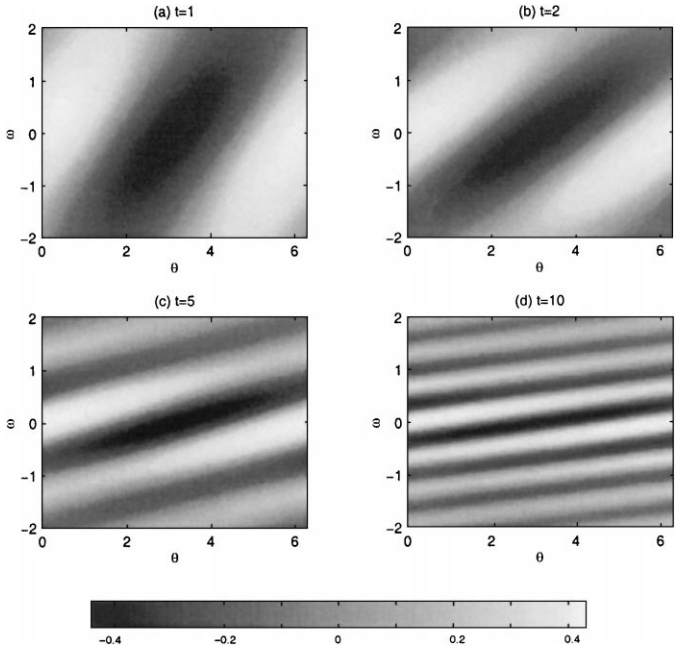

Fig. 3. Crenellating solution (23) to the linear initial-value problem with $K = 1.25$ at (a) $t = 1$, (b) $t = 2$, (c) $t = 5$ and (d) $t = 10$.

To understand the dynamics underlying the decay of the order function, and also to differentiate it from the decay of a normal mode, we must examine the probability density. For brevity, we do this in the special case $L = 0$, $K = 1$ and $a = 2$, for which

$$r(t) = \tfrac{10}{9}\mathrm{e}^{-t/2} - \tfrac{4}{9}\mathrm{e}^{-2t}, \tag{22}$$

$$c_1(\omega, t) = \left(\frac{2}{\pi}\frac{1}{\omega^2+4} - \frac{5}{9\pi}\frac{1}{2\mathrm{i}\omega-1} - \frac{1}{9\pi}\frac{1}{2-\mathrm{i}\omega}\right)\mathrm{e}^{-\mathrm{i}\omega t} + \frac{5}{9\pi}\frac{\mathrm{e}^{-t/2}}{2\mathrm{i}\omega-1} + \frac{1}{9\pi}\frac{\mathrm{e}^{-2t}}{2-\mathrm{i}\omega}. \tag{23}$$

Evidently, the function $c_1(\omega, t)$ contains the non-decaying and non-separable term $\mathrm{e}^{-\mathrm{i}\omega t}$, and hence cannot be described in terms of a normal mode. As time proceeds, this term becomes progressively more crenellated and, through increasing cancellations, integral averages of $c_1(\omega, t)$ decay. Because the order parameter is essentially such an integral average, r therefore decays in time.

The crenellation process is illustrated in Fig. 3 which displays four snapshots of the perturbation to the probability distribution as densities on the (θ, ω)-plane. The crenellation results from a tilting over of the initially vertical stripes of the pattern of the perturbation. The tilt itself arises from the evolving phase difference between oscillators with different frequencies. In other words, crenellation and continuum damping are just the phase mixing of the oscillator population.

4. Numerical schemes

The continuous model is most efficiently solved by Fourier decomposition in θ: $\rho = \sum_{m=-\infty}^{\infty}\tilde{\rho}_m(\omega, t)\mathrm{e}^{\mathrm{i}m\theta}$. For each value of ω, we truncate the Fourier series at $m = L$. We used L up to 512 in the computations; the smaller the dissipation or the longer the time of integration, the more Fourier modes are needed. For $D \geq 10^{-2}$ and stable

coupling strengths, we found that $L = 32$ was a good compromise in many situations. For smaller D, more Fourier modes are essential, and we used upto 512 for the computations with $D = 0$ and the largest initial probability densities. In the unstable cases, $L = 64$ was adequate for $D \geq 10^{-2}$. But for the non-diffusive computations we again used $L = 512$.

The simplicity of the truncated system above relies on the form of the mean-field interaction term; for more general $f(\theta)$, the equations are not tri-diagonal, but the generalization is straightforward.

To simplify the numerical computations, we considered frequency distributions with compact support on $[-1, 1]$. In particular, as an analgoue of the Lorentzian, we consider the probability density function

$$g(\omega) = \begin{cases} \dfrac{(1-\omega^2)}{[(\pi-2)(1+\omega^2)]} & \text{for } |\omega| < 1, \\ 0 & \text{for } |\omega| > 1. \end{cases} \tag{24}$$

The oscillator population with $|\omega| > 1$ then decouples from the problem and we may solve for the remainder of the population on the finite domain.

Following Crawford and Davies [3], we evaluate the integrals over ω using Gauss–Legendre quadrature, splitting the integration range into sub-intervals to improve resolution if necessary. This requires the values of ρ at a set of quadrature points, which is where we solve the ODEs for the Fourier decomposition. Almost always, we used 501 quadrature points. However, when the diffusivity was small, we used up to 1201 points. In all cases, we verified that resolution in both θ and ω was sufficient.

With the Fourier decomposition and Gaussian quadrature in hand, we integrate the system using a semi-implicit Adams–Bashforth–Moulton predictor–corrector scheme. In the predictor–corrector time integration, we extrapolate forwards for ρ at the beginning of the time-step. Given this approximation to ρ, we evaluate $G(\theta, t)$, and then correct ρ implicitly (which requires the inversion of a tri-diagonal matrix) to finish the time-step. This makes the scheme a semi-implicit one and ensures numerical stability.

In all the numerical integrations, we used the initial conditions

$$\rho(\theta, \omega, 0) = \frac{1}{2\pi} + \frac{2a}{\pi(\omega^2 + a^2)}\xi \cos(\theta + L\omega), \tag{25}$$

where L, a and ξ are constants. This starting distribution corresponds to the initial condition used to compute the solution of the linear initial-value problem in Section 3.2 (where $\xi \to 0$). Practically, we take $a = 2$. Because the initial density must be positive, the amplitude of the *kick* given to the system to knock it out of the steady state cannot exceed a maximum value: $\xi \leq \frac{1}{2}$.

Though we focus on the continuous version of the Kuramoto model, we also solve the discrete ODEs (1) to verify the correspondence of the two systems and to check that there are no special effects introduced by discreteness. The integration of the ODEs is performed with a fixed step ($\Delta t = 0.1$), fully implicit, predictor–corrector scheme when $D \neq 0$. The fixed time-step is forced by the noise term that prevents the convergence of adaptative methods. If $D = 0$, we use a more accurate and efficient variable step, Runge–Kutta scheme.

To parallel the initial condition used in the numerical integrations of the PDE, we first select the frequency of the jth oscillator from the $g(\omega)$-distribution in (24). Then, we choose the initial phase randomly from a distribution of the form (25) with $\omega = \omega_j$, $L = 0$, $a = 2$ and ξ suitably prescribed.

5. Nonlinear perturbations in stably incoherent populations

Before passing on to the transition to synchrony, we first consider finite-amplitude perturbations in stable populations. The aims are two-fold. First, the linear initial-value problem only captures the dynamics of disturbances of

infinitesimal amplitude, and it is not clear whether this property extends to disturbances of finite amplitude. Second, depending on the structure of the initial condition, one can find perturbations that grow for arbitrarily long intervals of time in the linear initial-value problem. This raises the important question of what happens to these disturbances when they enter the nonlinear regime.

5.1. Nonlinear continuum damping

One feature of the dynamics of fluid shear flows and plasmas is that nonlinear perturbations need not always crenellate and decay, despite the linear Landau damping. Given sufficient initial amplitude, perturbations can sustain themselves against tilting, wrap up the equilibrium distribution and again create a chain of cat's eyes [20–22]. In other words, continuum damping only proceeds if the initial amplitude is sufficiently small; otherwise, the flow evolves to structured patterns. Thus, pattern formation can occur even on perturbing stable equilibria in shears and plasmas. This poses the question of whether a similar effect arises in stable, noise-free oscillator populations — can nonlinearity halt the Landau damping? If so, structured patterns of synchrony could emerge even at sub-threshold coupling strengths provided the population is given a sufficiently strong initial perturbation.

In Fig. 4, we display numerical solutions for $\rho(\theta, \omega, t)$ at six successive instants of time, with initial condition (25) and $\xi = 0.1$. One of the curves in Fig. 5a displays the corresponding evolution of order parameter (equivalently, $|\mathcal{G}(t)|$). A tilting, periodic array of stripes of probability is evident, much like the solutions of the linear initial-value problem displayed earlier. In other words, the oscillators again phase mix and the finite-amplitude perturbation decays by continuum damping.

To determine whether nonlinearity has any effect on continuum damping, we performed a set of computations with varying ξ. The results are shown in Fig. 5. The oscillations that arise for long times and low amplitudes in

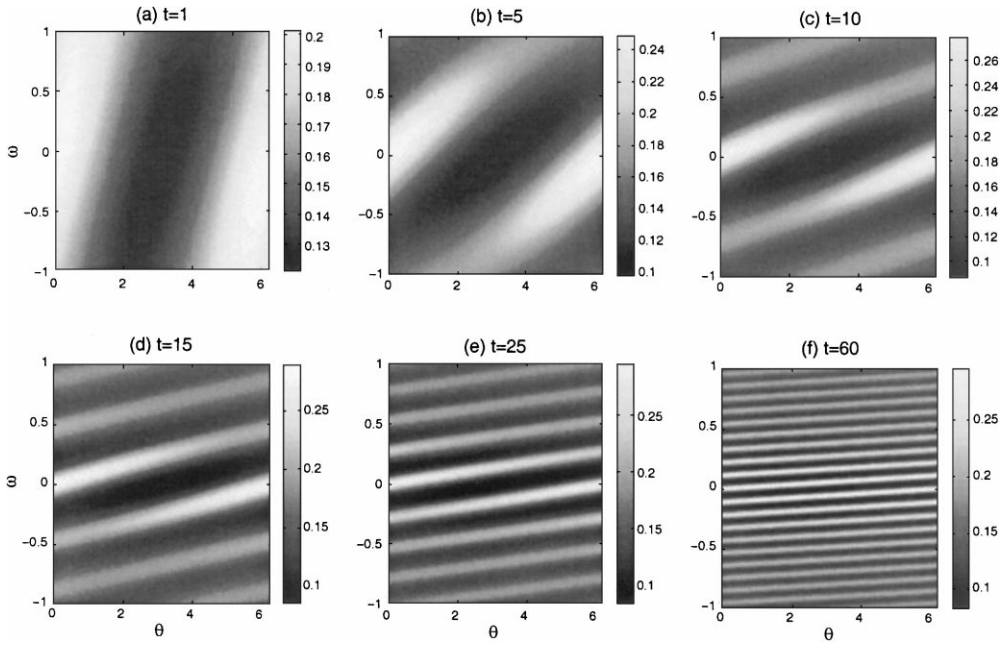

Fig. 4. $\rho(\theta, \omega, t)$ at six successive instants of time obtained via numerical integration with frequency distribution (24), initial condition (25), and $D = 0$, $\xi = 0.1$, $K = 0.5$, $a = 2$ and $L = 0$ ($K_c = 0.727$).

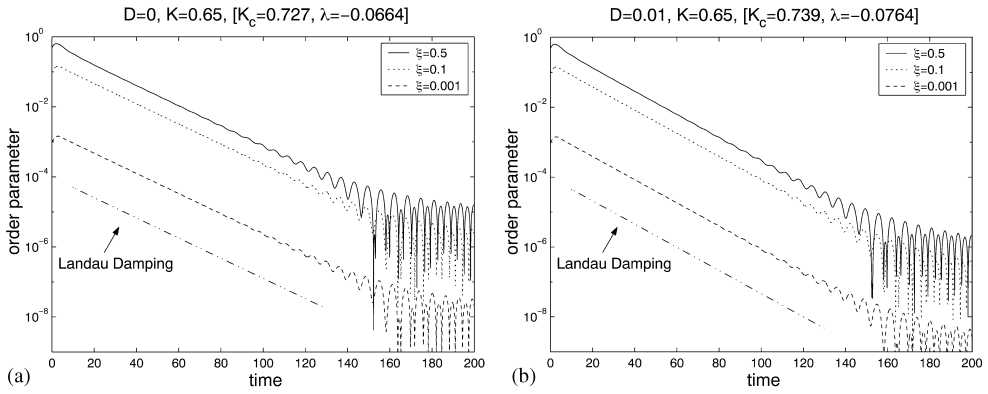

Fig. 5. Time evolution of the order parameter for the Kuramoto continuous model with frequency distribution (24) and initial condition (19). Several stable, noisy cases are displayed with $K = 0.65$. In panel (a), with $D = 0$, we show cases with $\xi = 10^{-3}$, 0.1 and 0.5; the dashed-dotted line shows the trend of Landau damping. Panel (b) shows the same picture, but for $D = 0.01$. $a = 2$ and $L = 0$.

this figure are due to the finite computational domain, which limits the continuous spectrum to a finite cut on the spectral plane [17]. The oscillations have a period of $2\pi d$, where d is the maximum coupled frequency (in this case $d = 1$).

Even for the biggest kick, with $\xi = \frac{1}{2}$, there is no significant difference between the decay of the order parameter and the linear Landau damping. Thus no new, nonlinearly induced phenomena apparently occur. This is quite unlike the fate of nonlinear perturbations in inviscid fluid shears and ideal plasmas. However, the information contained in the order parameter misses a *bona fide* nonlinear effect.

We observe this effect by looking at the probability distribution. As illustrated in Fig. 6, when ξ is relatively large, the probability collects into narrow regions and disappears from large portions of the (θ, ω)-plane. This creates a sharply peaked distribution which indicates that the oscillator population shows significant synchronization even below the critical threshold. The synchronization is much more pronounced than one expects from linear theory, as illustrated in Fig. 7 which shows the peak values of ρ for $\xi = 0.5$. (However, with the larger values of ξ, linear theory predicts negative probability densities.) The larger nonlinear densities arise through two effects. First, the peaks of the probability distribution sharpen through a nonlinear focussing effect. Second, the depletion of probability between the peaks creates flat plateaus of negligible density.

5.2. Transient amplification

The possibility of unlimited transient amplification in the linear initial-value problem can be seen from the solution considered in Section 3.2. There, for $t < L$, the order parameter grows exponentially (see Fig. 2). These transiently amplifying perturbations are inclined backwards with respect to the intrinsic phase evolution of the oscillators. As a result, they tilt forwards to *un-crenellate* the distribution for a time. Ultimately, the perturbation decays, but, in the interim, integral averages such as the order parameter may grow by many orders of magnitude. This is analogous to the classical shear-tilting mechanism of Kelvin and Orr in fluid mechanics, which has recently been brought back into fashion with the rejuvenated idea that such tilting perturbations may rise to sufficiently large amplitude to enter the nonlinear regime and spark the transition to turbulence in pipe and channel flows [23]. Physically, for our coupled oscillators, transient amplification corresponds to a brief flash of coherence in the population before it lapses to asynchrony. But, such amplification may induce nonlinear disturbances and produce sustained coherence in the population for coupling strengths below the critical threshold.

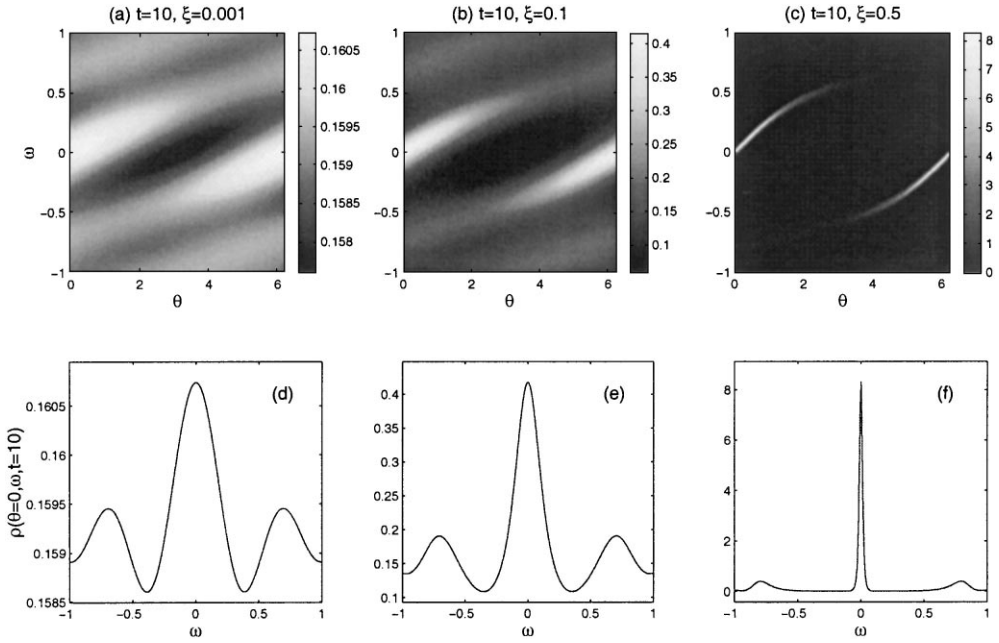

Fig. 6. $\rho(\theta,\omega,t)$ at $t=10$ for three different numerical integrations with frequency distribution (24) and initial condition (25), $D=0$ and $K=0.65$ ($K_c=0.727$). Panels (a)–(c) show $\xi=10^{-3}$, 0.1 and 0.5, respectively. Panels (d)–(f) show slices through the probability density at $\theta=0$. $a=2$ and $L=0$.

To explore this possibility, we numerically integrated the PDE with the initial condition (25) and $L=40$. The resulting evolution of the order parameter is shown in Fig. 8. As for the linear solution, the order parameter grows by orders of magnitude before decaying. But, the ultimate behaviour is still the decay predicted by linear theory. There are two notable differences between the linear solution and the nonlinear integration. First, for small times, the order parameter oscillates at a level of about 10^{-4} rather than rising from much lower values. Second, oscillations also set in for large times. Both effects result from the finiteness of the computational domain (and, eventually, the resolution) and not from nonlinearity.

Transient amplification does not therefore lead to an entry of the system into the nonlinear regime and the creation of sustained synchrony. Indeed, the only apparent effect of nonlinearity is to focus and sharpen the peaks in the

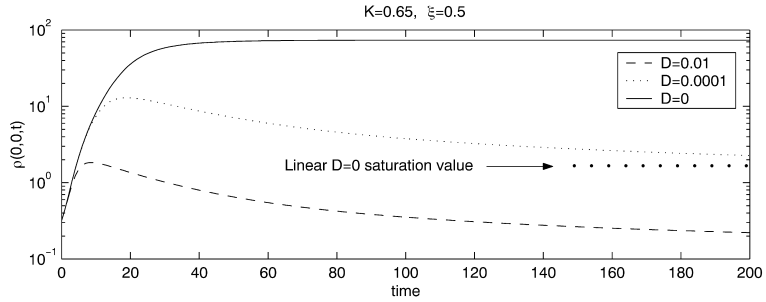

Fig. 7. Time evolution of the peak value of $\rho(\theta,\omega,t)$. Three noisy stable cases are displayed with $D=0$, 0.0001 and 0.01, for $K=0.65$, $\xi=0.5$ and $L=0$. The dots show the peak value expected from linear theory with $D=0$, $a=2$ and $L=0$.

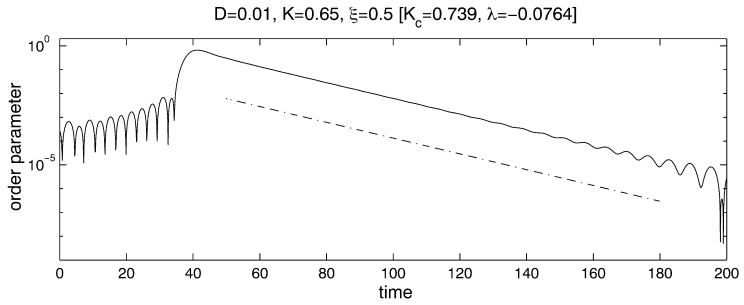

Fig. 8. Time evolution of the order parameter. A noisy stable case is displayed with $D = 0.01$, $K = 0.65$, $\xi = 0.5$, $a = 2$ and $L = 40$ ($K_c = 0.739$). The broken line shows the expected linear decay rate.

probability distribution as for nonlinear continuum damping. Whilst this heightens the amount of synchrony in the population over intermediate times, it does not alter the ultimate coarse-grained decay to incoherence. Instead, we must look to unstable populations to observe longlived coherence.

6. A vision of synchronization

In this section, we begin our discussion of sustained synchronization and describe numerical integrations of unstable populations. One such integration is illustrated in Figs. 9 and 10, which shows the order parameter, and snapshots of $\rho(\theta, \omega, t)$ on the (θ, ω)-plane.

In Fig. 10, the probability initially gathers into tilting stripes. However, rather than continually tilting, phase mixing ends and the stripes evolve into a quasi-steady pattern in which probability gradually collects into two regions and depletes elsewhere. The probability distribution evolves into a finer structure in these special regions, as illustrated in Fig. 11 (the evolution of the order parameter corresponding to this integration is shown in Fig. 12). This shows how fine scales develop inside a "critical region" much like how structure forms inside the critical layer of an unstable mode in an ideal plasma or shear flow. However, the geometry is quite different from a cat's eye pattern.

As fine structure develops in the critical region, the peak probability density increases dramatically (see Figs. 11 and 13a). The peak amplitude (occurring at $\omega = \theta = 0$) eventually levels off at a value dictated by the degree of noise (Fig. 13b); for $D \to 0$, the peak amplitude appears to increase without saturation (the peak never diverges in the

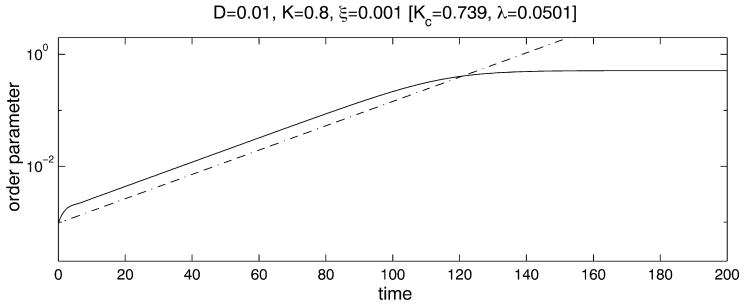

Fig. 9. Time evolution of the order parameter. An unstable noisy case is shown with $D = 0.01$, $K_c = 0.739$, $\xi = 0.001$ and $K = 0.8$. The broken line shows the expected linear growth rate. $a = 2$ and $L = 0$.

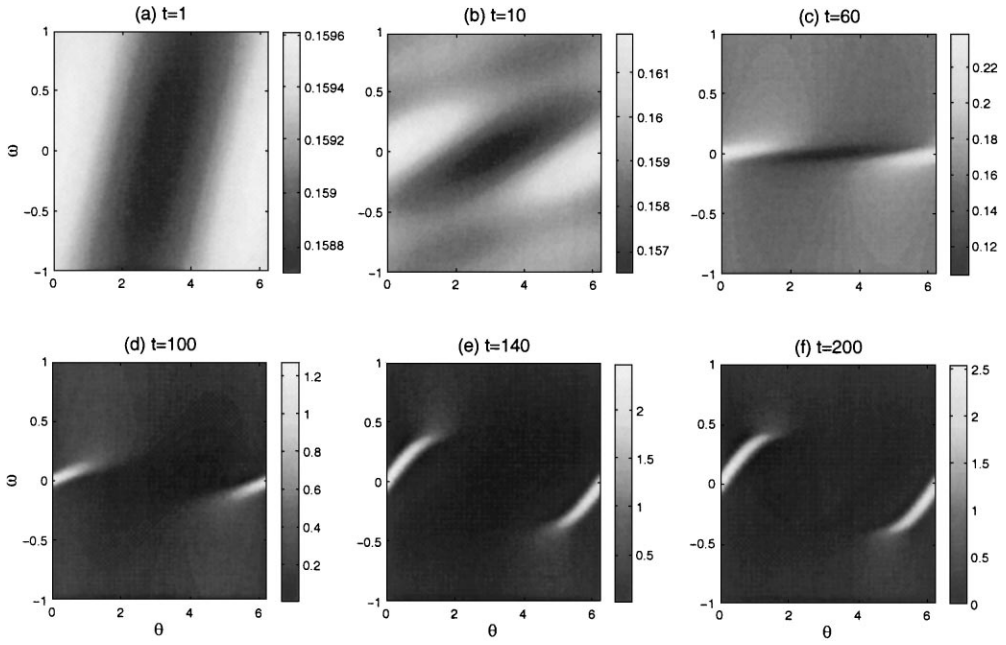

Fig. 10. $\rho(\theta, \omega, t)$ at six successive instants of time obtained via numerical integration, and corresponding to Fig. 9.

computations due to artifical diffusion caused by finite resolution). Also, although the peak probability may diverge as $D \to 0$, the order parameter shows no such singular behaviour and, in fact, approaches a level independent of D (see Fig. 12). Both of these observations are consistent with the boundary-layer theory presented in Section 7.2 that constructs steady solutions to the PDE. The predictions of the asymptotic theory are included in Figs. 12b and 13b.

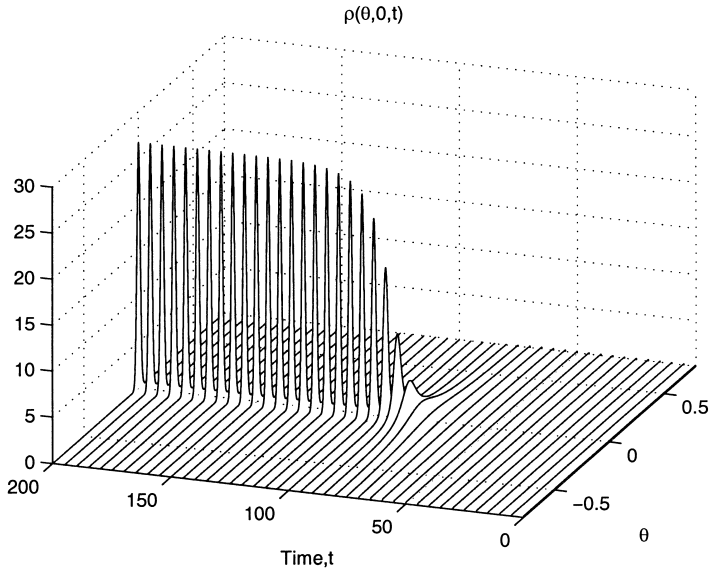

Fig. 11. Snapshots of $\rho(\theta, 0, t)$ drawn above the (θ, t)-plane for a numerical integration with $K = 0.8$, $D = 10^{-4}$, $a = 2$, $L = 0$ and $\xi = 0.001$.

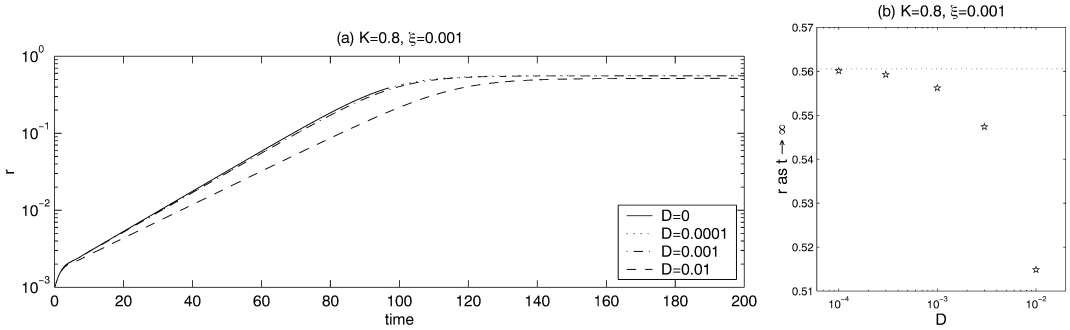

Fig. 12. (a) Time evolution of the order parameter for numerical integrations with $K = 0.8$, $a = 2$, $L = 0$ and $\xi = 0.001$. Four values of D are shown. For $D = 0$, the computation becomes unreliable just below $t = 100$ and is not plotted thereafter. (b) Final value of r as a function of D. The line shows the value expected from the boundary-layer theory of Section 7, as given by (41).

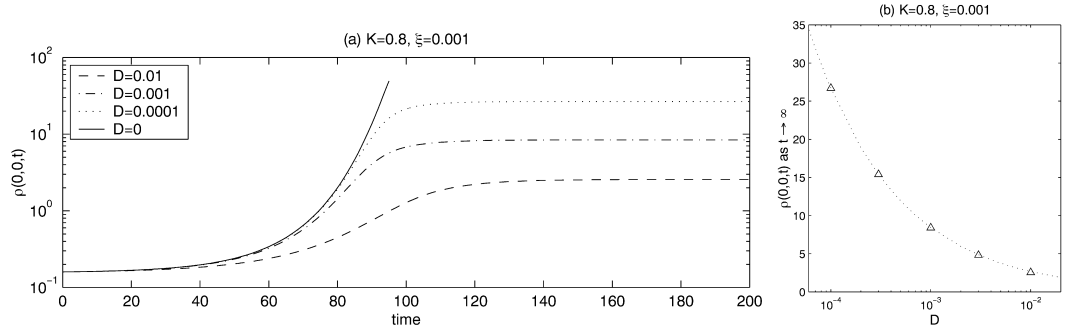

Fig. 13. (a) Time evolution of the peak of the probability distribution for the same numerical integrations as in Fig. 12. Again, the $D = 0$ case is halted when the code becomes unreliable. (b) Final peak value as a function of D. The curve shows the value expected from the boundary-layer theory of Section 7, as given by (37).

Because the probability density develops ever finer and higher peaks in populations with very low noise levels, a cascade to smaller scales occurs as evolution proceeds. As a result, the accuracy of the numerical scheme ultimately breaks down when the width of the peak reaches the wavelength of the highest Fourier mode. This is illustrated in Fig. 14; the two cases with $D = 0.01$ and 10^{-4} are resolved, but for $t > 100$, the $D = 0$ computation is not reliable. (Note the large number of Fourier modes used in this particular computation.) The cascade makes long-time computations especially difficult in the noise-free limit.

The phenomenology of the supercritical evolution for noise-free populations is reminiscent of the formation of an irregular solution. Indeed, the "potential" u, defined by $u_\theta = \rho$, evolves towards an almost discontinuous profile much like a shock layer. This is, perhaps, not so surprising in view of similarities between the equation satisfied by u and Burger's equation. We give further analogies with shock formation later.

7. Steadily oscillating populations

A feature of the numerical simulations illustrated above is that, when $K > K_c$ and $D \neq 0$, the population evolves to a steady solution in which $\mathcal{G}$ becomes constant and ρ approaches a stationary pattern. If $D = 0$, there is some suggestion that $\mathcal{G}$ again levels off, but ρ appears to focus continually into special regions. This motivates a search for

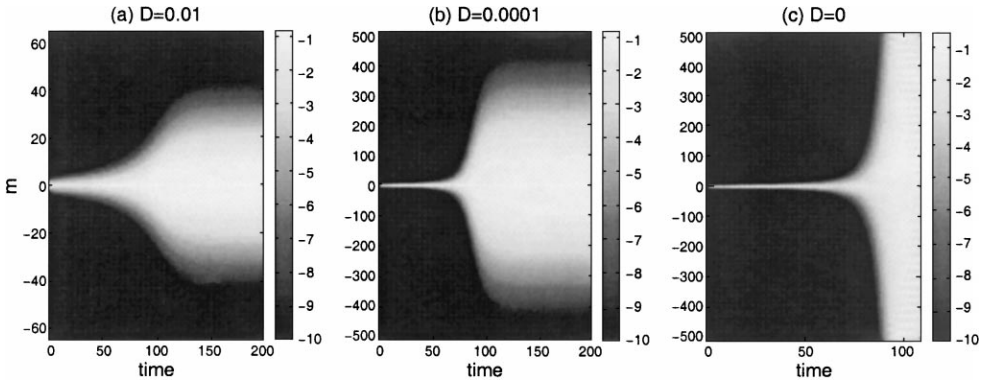

Fig. 14. This figure shows the amplitude of the Fourier modes, $|c_m(\omega, t)|$, as a density on the (t, m)-plane at $\omega = 0$ for numerical integrations with $K = 0.8$, $a = 2$, $L = 0$ and $\xi = 0.001$. The greyscale is logarithmic, as given by the key. The three panels are for (a) $D = 0.01$, (b) $D = 10^{-4}$ and (c) $D = 0$. Note that different resolutions are used in the three cases.

steady solutions of the PDE. More generally, these particular solutions are special examples of steadily oscillating populations in which $G(\theta, t)$ and $\rho(\theta, \omega, t)$ take the form of rigidly "rotating" or "propagating" patterns in phase. In this section, we look for these steadily propagating solutions.

7.1. The absence of silent smooth solutions

The steadily propagating solutions take the form,

$$\rho(\theta, \omega, t) = \rho(\theta - \Omega t, \omega) \equiv \rho(\Theta, \omega) \quad \text{and} \quad G(\theta, t) = G(\theta - \Omega t) \equiv G(\Theta), \tag{26}$$

where Ω is the propagation velocity and $\Theta = \theta - \Omega t$.

Eq. (5), for $D = 0$, becomes

$$(\omega - \Omega)\rho_\Theta + K(G\rho)_\Theta = 0. \tag{27}$$

On integrating in Θ:

$$\rho = \frac{\mathcal{J}(\omega)}{\omega - \Omega + KG}, \tag{28}$$

where $\mathcal{J}(\omega)$ is an arbitrary function of ω. But, as a probability density, ρ cannot have a non-integrable singularity. Yet, because ω is a real variable that spans the entire real axis, the pole from the denominator of ρ is hard to avoid. This is an interesting point: if the dissipation is zero the system does not admit steadily propagating, smooth solutions with $r > 0$. However, there are solutions when the dissipation is finite, but small, and there are irregular solutions with $D = 0$, as we show in the next section.

7.2. Noisy boundary layers

If $D \neq 0$, we have

$$(\omega - \Omega + KG)\rho = \mathcal{J}(\omega) + D\rho_\Theta. \tag{29}$$

As indicated above, because there is always a curve on the (Θ, ω)-plane for which $\omega - \Omega + KG = 0$, or $\Theta = \Delta(\omega)$, we cannot neglect the dissipative term in this equation. This curve lies inside the frequency interval, $[\omega_1, \omega_2] \equiv [\Omega - KG_{\max}, \Omega - KG_{\min}]$, which we refer to as the *synchronizing zone*.

If $\Omega - KG_{\min} < \omega$ or $\omega < \Omega - KG_{\max}$, we are outside the synchronizing zone and there is no pole in the noise-free solution (28). Here, if $D \ll 1$, we may ignore the noise term and adopt that solution. Moreover, normalizing as in Eq. (7) gives

$$\mathcal{J}(\omega) = \left[\int_{-\pi}^{\pi} \frac{\mathrm{d}\Theta}{\omega - \Omega + KG(\Theta)}\right]^{-1}. \tag{30}$$

On the other hand, where $\Omega - KG_{\max} < \omega < \Omega - KG_{\min}$, there is a value of $\Theta = \Delta(\omega)$ for which the noise-free solution (28) diverges. In the vicinity of this special angle, $\rho \sim 1/(\Theta - \Delta)$, and we cannot ignore the dissipative term. This sets the stage for a boundary-layer calculation of the solution.

Inside the noisy boundary layer, we set

$$\Theta - \Delta = \delta\sqrt{D} \quad \text{and} \quad \rho = \frac{1}{\sqrt{D}} R. \tag{31}$$

On substituting in Eq. (29) and noting that $\partial_\Theta = D^{-1}\partial_\delta$, we find that, to leading order

$$KG_\Theta(\Delta)\delta R = \mathcal{J}(\omega) + R_\delta. \tag{32}$$

Hence

$$R = \mathrm{e}^{KG_\Theta\delta^2/2}\left[\mathcal{N} - \mathcal{J}\int_0^\delta \mathrm{e}^{-KG_\Theta\bar{\delta}^2/2}\,\mathrm{d}\bar{\delta}\right] \equiv \mathrm{e}^{KG_\Theta\delta^2/2}\left[\mathcal{N} - \mathcal{J}\mathrm{Erf}\left(\delta\sqrt{\frac{KG_\Theta}{2}}\right)\sqrt{\frac{\pi}{2KG_\Theta}}\right], \tag{33}$$

where $\mathcal{N}(\omega)$ is another arbitrary function and we omit the argument from $G_\Theta(\Delta)$.

We next demand that, for $|\delta| \to \infty$, $R(\delta, \omega)$ matches with the "inner" limit of the outer, noise-free solution, $\rho \sim \mathcal{J}/[KG_\Theta(\Delta)(\theta - \Delta)]$. By using the asymptotics of the error function, it is straightforward to see that the only possible way in which we can perform this matching is to take $\mathcal{J} = 0$. Moreover, we must further take $\mathcal{N} = 0$ if $G_\Theta > 0$. This leaves us with an exponentially localized, Gaussian boundary-layer solution in the vicinity of that part of the curve $\omega = \Omega - KG(\Theta)$ for which $G_\Theta < 0$. Fig. 15 shows a sketch of the situation for $\Omega = 0$.

The value of $\mathcal{N}(\omega)$ for $G_\Theta(\Delta) < 0$ is computed using the normalization condition (7):

$$\mathcal{N} = \left[\int_{-\infty}^{\infty} \mathrm{e}^{-K|G_\Theta|\delta^2/2}\,\mathrm{d}\delta\right]^{-1} \equiv \sqrt{\frac{K|G_\Theta|}{2\pi}}. \tag{34}$$

To complete the construction of the solution, we need only to evaluate the integral determining G. This integral constraint provides a relation that determines the order function, given K. Because the contribution of the noise-free solution (73) from outside the synchronizing zone vanishes, the integral is limited to the boundary layer, and

$$G(\Theta, t) = \int_{-\infty}^{\infty}\int_0^{2\pi} \sin(\Phi - \Theta)\rho(\Phi, \omega)g(\omega)\,\mathrm{d}\Phi\,\mathrm{d}\omega \approx \int_{\omega_1}^{\omega_2} \sin[\Delta(\omega) - \Theta]g(\omega)\,\mathrm{d}\delta\,\mathrm{d}\omega. \tag{35}$$

D does not enter this expression, and so the order parameter becomes independent of the noise level in the limit.

To summarize, steadily propagating solutions cannot develop for $D = 0$; with D finite, but small, there are solutions with noisy boundary layers that follow the line $\omega - \Omega + kG(\Theta) = 0$, where $G_\Theta(\Delta) < 0$.

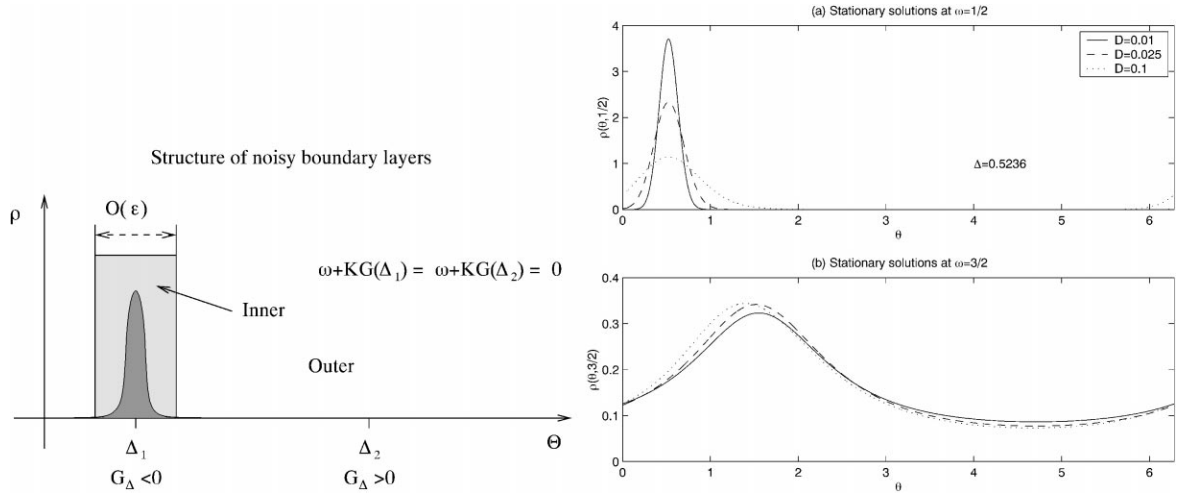

Fig. 15. Steadily propagating solutions. The left-hand panel shows a sketch of $\rho(\Theta,\omega)$. There is a special curve $\Theta=\Delta$, where $\omega+KG(\Delta)=0$, which locates the boundary layer. Due to the periodicity of $G(\Theta)$, there are two locations in Θ for each ω inside the synchronizing zone, Δ_1 and Δ_2. Only one of these has $G'(\Delta)<0$ (Δ_1 is chosen to have $G'(\Delta_1)<0$ in the sketch), and in the vicinity of this location, there is a noisy boundary layer (*light grey region*) in which the solution is exponentially localized. Above and below the synchronizing zone, the solutions are essentially noise-free. The structure is illustrated in detail in the right-hand side panels which show steady solutions computed for $K\mathcal{G}=1$, three different values of D and (a) $\omega=\frac{1}{2}$ (inside the synchronizing zone, with boundary-layer structure) and (b) $\omega=\frac{3}{2}$ (outside the synchronizing zone, with structure approximately independent of D).

7.3. Symmetrical stationary solutions

By way of example, we consider symmetrical stationary solutions, $\Omega=0$. In this case, the solution is concentrated around that part of the line $\omega=K\mathcal{G}(t)\sin\theta$ with $\mathcal{G}\cos\theta>0$:

$$\rho\approx\begin{cases}\dfrac{\sqrt{\omega^2-K^2\mathcal{G}^2}}{[2\pi(\omega-K\mathcal{G}\sin\theta)]} & \text{for } \omega^2>K^2\mathcal{G}^2,\\[2ex] \left[\dfrac{(K^2\mathcal{G}^2-\omega^2)}{4\pi^2D^2}\right]^{1/4}\exp\left(-\dfrac{\delta^2\sqrt{K^2\mathcal{G}^2-\omega^2}}{2}\right)H(\mathcal{G}\cos\theta) & \text{for } \omega^2<K^2\mathcal{G}^2,\end{cases}\tag{36}$$

where $H(x)$ denotes the Heaviside function. Note that the two formulae are not consistent in the vicinity of $\omega=K\mathcal{G}$ and $\theta=\pm\pi/2$. Strictly speaking, in those regions, which surround the "tips" of the special curve $\omega=K\mathcal{G}\sin\theta$, we need a different asymptotic expansion (see Section 8). However, to determine the leading-order form of the solution it is not necessary to uncover these technical details.

In Fig. 16, the special curve is superimposed on a numerical solution, using the steady value of $\mathcal{G}$ approached at the end of the computation. The probability collects in exactly the region predicted. The exponential localization of the steady solution to the boundary layer also explains the depletion of probability in the middle of the (θ,ω)-plane. It is straightforward to read off the peak probability density from (36):

$$\rho_{\max}\approx\sqrt{\frac{K\mathcal{G}}{2\pi D}},\tag{37}$$

which agrees with the results of numerical integration (see Fig. 13).

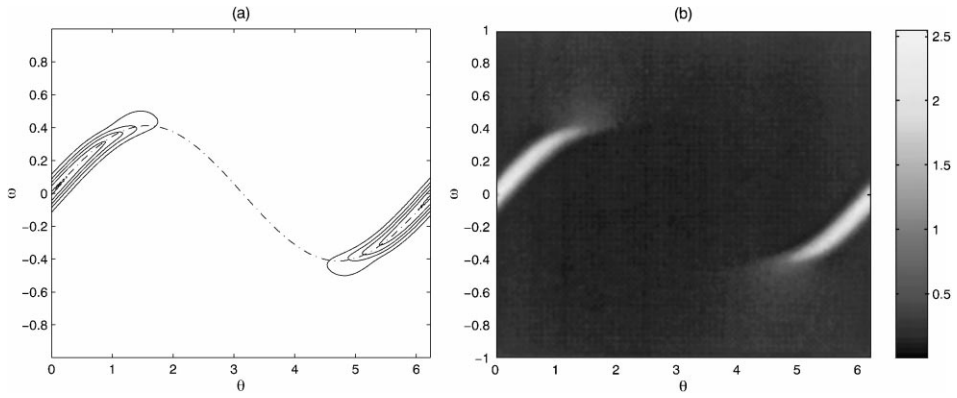

Fig. 16. $\rho(\theta,\omega,t)$ at $t = 180$ obtained via numerical integration (see Fig. 9 for further details). In panel (a) we superimpose the line, $\omega = K\mathcal{G}\sin(\theta)$, on a contour plot of ρ, where $\mathcal{G}$ is set to the final, steady value obtained in the integration.

For general values for D, we may explicitly integrate the dissipative equation:

$$\rho = \frac{\mathcal{J}(\omega)}{D}\mathrm{e}^{p(\theta,\omega)}\left[P(\theta,\omega) + \frac{\mathrm{e}^{-2\pi\omega/D}}{1-\mathrm{e}^{-2\pi\omega/D}}P(0,\omega)\right], \tag{38}$$

where $\mathcal{J}(\omega)$ must be fixed by the normalization

$$p(\theta,\omega) = \frac{1}{D}(\omega\theta + K\mathcal{G}\cos\theta) \quad \text{and} \quad P(\theta,\omega) = \int_{\theta}^{2\pi}\mathrm{e}^{-p(\theta',\omega)}\,\mathrm{d}\theta'. \tag{39}$$

Solutions for $K\mathcal{G} = 1$ are shown in Figs. 15 and 17. In Fig. 17, the solution is not computed consistently by using (35) to determine $\mathcal{G}$ at the same time as constructing ρ. Instead, we construct ρ for fixed $K\mathcal{G}$, and then compute the integral for $\mathcal{G}$, which finally gives the corresponding coupling strength K. (For the two cases shown in the figure, $D = 0.01$ and $K \approx 2.4$ in panel (a), and $D = 0.1$ and $K \approx 2.6$ in panel (b).) This technique can be used to construct numerically the locus of dissipative solution branches, $\mathcal{G} = \mathcal{G}(K)$; a selection is shown in panel (c). The branches bifurcate from the incoherent solution at the critical coupling strength, as expected from the dissipative, weakly nonlinear theory, and the structure of the solutions is comparable to the end states of numerical integrations.

By using the boundary-layer form for ρ, we may also compute the integral in (35):

$$\mathcal{G} \approx \int_{-K\mathcal{G}}^{K\mathcal{G}} g(\omega)\,\mathrm{d}\omega\sqrt{1-\frac{\omega^2}{K^2\mathcal{G}^2}}\int_{-\infty}^{\infty}\mathcal{N}\mathrm{e}^{-\delta^2\sqrt{K^2\mathcal{G}^2-\omega^2}/2}\,\mathrm{d}\delta = \int_{-K\mathcal{G}}^{K\mathcal{G}} g(\omega)\,\mathrm{d}\omega\sqrt{1-\frac{\omega^2}{K^2\mathcal{G}^2}}. \tag{40}$$

For our compact distribution (24),

$$\mathcal{G} \approx \frac{\sqrt{8(K-2+4/\pi)/K}}{(K+2-4/\pi)}, \tag{41}$$

which is compared with the results of numerical integrations in the previous section (see Fig. 12). For the Lorentzian,

$$\mathcal{G} \approx \sqrt{1-2/K}, \tag{42}$$

which is identical to Kuramoto's solution (see Section 1). This equivalence raises the question of what Kuramoto's noise-free solutions correspond to in the PDE, a question we answer in Section 7.4.

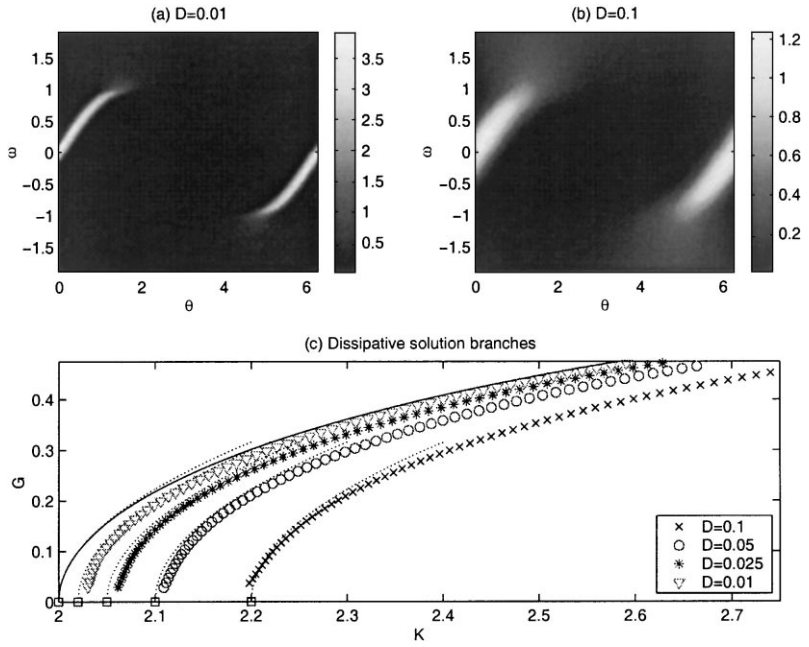

Fig. 17. Dissipative steady solutions for (a) $D = 0.01$ and (b) $D = 0.1$, with $K\mathcal{G} = 1$. Panel (c) locates the dissipative solution branches on the $(K, \mathcal{G})$ plane for four values of D. The squares show the bifurcation points, $K_c = 2 + 2D$. The solid curve is Kuramoto's solution (42). The dotted curves show the weakly nonlinear solution derived in Section 8.1, which assume significant noise. Near the bifurcation, the numerical scheme becomes inaccurate.

7.4. Irregular solutions

Another possible solution to (28) is the distribution

$$\rho = \begin{cases} K|G_\Theta(\Delta)|\delta(\omega - \Omega + KG)H(-G_\Theta) & \text{for } \omega_1 < \omega < \omega_2, \\ \dfrac{\mathcal{J}(\omega)}{(\omega - \Omega + KG)} & \text{elsewhere,} \end{cases} \tag{43}$$

which corresponds to an integrably singular probability density along our special curve, together with an essentially noiseless density outside the synchronizing zone. This irregular solution is also the $D \to 0$ limit of the noisy structures described above, and corresponds exactly to Kuramoto's solution given in (3). The singular distribution simply represents the sub-population of perfectly synchronized oscillators.

The irregular stationary solutions are given by

$$\rho = \begin{cases} \sqrt{K^2\mathcal{G}^2 - \omega^2}\,\delta(\omega - K\mathcal{G}\sin\theta)H(\cos\theta) & \text{for } -K\mathcal{G} < \omega < K\mathcal{G}, \\ \dfrac{\sqrt{\omega^2 - K\mathcal{G}^2}}{[2\pi(\omega - K\mathcal{G}\sin\theta)]} & \text{elsewhere.} \end{cases} \tag{44}$$

Once again, the only contribution to the integral determining $\mathcal{G}$ arises from the synchronized portion of the population, and so

$$1 = K\int_{-\pi/2}^{\pi/2} \cos^2\Phi\, g(K\mathcal{G}\sin\Phi)\,\mathrm{d}\Phi. \tag{45}$$

For the Lorentzian, the integral may be explicitly evaluated to give the familiar result, $\mathcal{G} = \sqrt{1 - 2/K}$.

Thus, although there are no smooth stationary solutions to the noise-free Kuramoto model, there are irregular solutions with an obvious correspondence to weakly dissipative structures. Moreover, the numerical integrations described earlier suggest a dynamical evolution to structures of this kind.

8. Weakly nonlinear analysis and critical layer theory

The appearance of slender regions in which the solution develops fine scales is reminiscent of the formation of critical layers in ideal plasmas and shear flows. This motivates a weakly nonlinear expansion in which matched asymptotics are exploited to resolve critical level singularities. However, when D is not small, the matched asymptotics are not necessary and weakly nonlinear theory proceeds in a standard way; we summarize this case first. On appreciating how the theory breaks down when $D \to 0$, we sketch out the critical-layer analysis.

8.1. Dissipative theory

When $K = K_c$ and $D \neq 0$, one can derive a Landau equation for the amplitude of the marginally unstable mode [9,10]. The weakly nonlinear expansion proceeds as follows. With $\epsilon \ll 1$, a parameter organizing the expansion, let

$$\epsilon^2 t = T \quad \text{or} \quad \partial_t = \epsilon^2 \partial_T, \quad K = K_c + \epsilon^2 K_2 + \cdots, \tag{46}$$

$$\rho = \frac{1}{2\pi} + \epsilon[a(T)\hat{\rho}_1(\omega)\,\mathrm{e}^{\mathrm{i}\theta} + \text{c.c.}] + \epsilon^2\rho_2 + \epsilon^3\rho_3 + \mathrm{O}(\epsilon^4), \tag{47}$$

$$G = \epsilon G_1 + \epsilon^2 G_2 + \cdots, \tag{48}$$

where T is a slow time on which amplitude growth occurs, and $\hat{\rho}_1(\omega)$ denotes the neutral eigenmode with amplitude, $a(T)$. The scalings in these formulae are "Hopf scalings", suitable for unfolding the bifurcation of complex conjugate mode pairs.

From Eqs. (5) and (6) at first order ($\mathrm{O}(\epsilon)$), it follows that we may take

$$\hat{\rho}_1 = \frac{K_c}{2(\omega - \mathrm{i}D)} \quad \text{and} \quad \int_{-\infty}^{\infty} \hat{\rho}_1(\omega) g(\omega)\,\mathrm{d}\omega = 1. \tag{49}$$

These relations are consistent by virtue of the definition of K_c and $\hat{\rho}_1$. Continuing on, and in particular to $\mathrm{O}(\epsilon^3)$, one derives the amplitude equation

$$a_T = \tfrac{1}{2}K_2 a + (K_c\pi)^2 \mathcal{I}|a|^2 a, \tag{50}$$

where

$$\mathcal{I} = \int_{-\infty}^{\infty} \frac{\hat{\rho}_1 g(\omega)}{\omega - 2\mathrm{i}D}\,\mathrm{d}\omega. \tag{51}$$

From the Landau equation, we can construct the steady, dissipative solutions near the onset of synchrony. These must satisfy

$$|a|^2 = -\frac{K - K_c}{2\pi^2 K_c^2 \mathcal{I}}. \tag{52}$$

Moreover, to leading order, $\mathcal{G} \approx 2\pi|a|$. Hence, for the Lorenztian,

$$\mathcal{G} \approx \frac{\sqrt{(1+2D)(K/2-1-D)}}{(1+D)}. \tag{53}$$

This approximation is also drawn in Fig. 17.

We can see from the expression for ρ_1 that the approach breaks down when $D = 0$; ρ has a pole at $\omega = 0$, but as a probability density, this cannot have any physical meaning and must be avoided. At higher order, the situation becomes progressively worse, with even stronger singularities appearing in the solution. These singularities all occur at the critical level and signify the breakdown of standard weakly nonlinear theory in a system with a critical layer.

8.2. Consequences of Hopf scaling in the low-noise limit

In this section, we sketch the asymptotic expansion for the case $1 \gg D \neq 0$. We choose the variables to scale as in the previous case (Hopf scaling) but take $D = \epsilon^3 D_3$. The motivation for Hopf scaling can be found in our numerical experiments and in the analyses of Daido [4] and Crawford and Davies [3]. The scaling of D constitutes a distinguished limit, and ensures that the noise level enters the asymptotic expansion exactly where we want it.

On substituting the scalings into the governing equations, we find

$$\omega\rho_\theta + \epsilon^2\rho_T + (\rho G)_\theta(K_c + \epsilon^2 K_2) = \epsilon^3 D_3\rho_{\theta\theta}. \tag{54}$$

We solve this equation by introducing the expansion $\rho = 1/(2\pi) + \epsilon\rho_1 + \epsilon^2\rho_2 + \cdots$. At the first and second order, we derive expressions for ρ_1 and ρ_2 :

$$\mathrm{O}(\epsilon): \quad \rho_1 = -\frac{K_c G_1}{2\pi\omega}, \tag{55}$$

$$\mathrm{O}(\epsilon^2): \quad \rho_2 = \frac{K_c^2 G_1^2}{2\pi\omega^2} - \frac{K_c G_2}{2\pi\omega}. \tag{56}$$

Here, we immediately see the "critical-level" problem: the solution at both orders diverges as $\omega \to 0$. Moreover, for $\omega \sim \epsilon$, $\epsilon\rho_1$ and $\epsilon^2\rho_2$ are of similar magnitude, indicating that the asymptotic sequence becomes disordered in a slender region near $\omega = 0$. In this "critical layer", we must search for another solution.

Inside the critical layer, we use the new independent and dependent variables, $\omega = \epsilon y$ and $\rho = Z(\theta, y, T) = Z_0 + \epsilon Z_1 + \cdots$. The equation then becomes

$$\epsilon^2 Z_T + \epsilon y Z_\theta + (ZG)_\theta(K_c + \epsilon^2 K_2) = \epsilon^3 D_3 Z_{\theta\theta}. \tag{57}$$

At the first two orders,

$$\mathrm{O}(\epsilon): \quad (y + K_c G_1)Z_0 = \mathcal{J}_0(y, T), \qquad \mathrm{O}(\epsilon^2): \quad [(y + K_c G_1)Z_1]_\theta = -Z_{0T} - (Z_0 G_2)_\theta K_c,$$

where $\mathcal{J}_0(\omega, T)$ is currently undetermined.

Despite our attempt to regularize the singularities by including the critical layer, problems still remain: near $y + K_c G_1 = 0$, $Z_0 \sim 1/(y + K_c G_1)$ and $Z_1 \sim 1/(y + K_c G_1)^2$. Thus the first inner layer is not sufficient to avoid critical-level problems and it is necessary to include another critical region inside the first, much like a nested boundary layer. The inner layer has a non-trivial shape given by the θ-dependence of $G(\theta, T)$ and is sketched in Fig. 18.

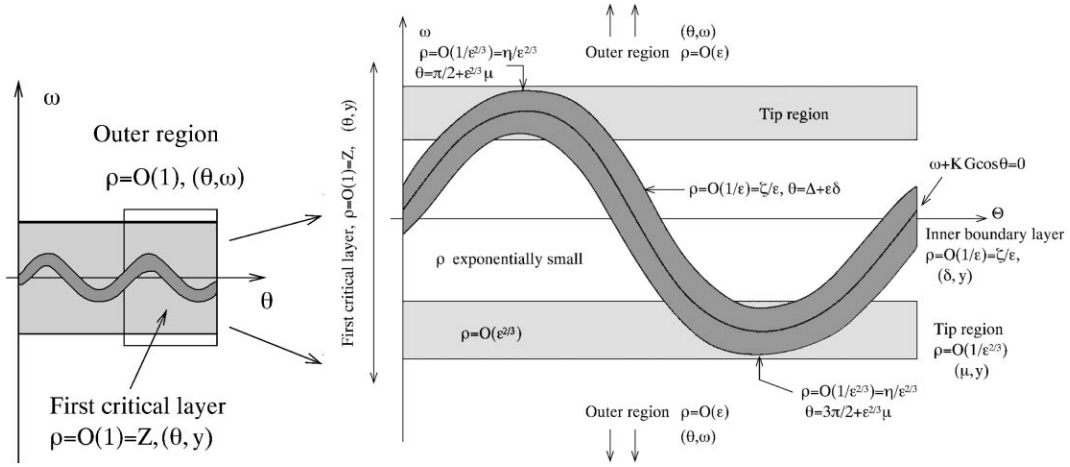

Fig. 18. For small dissipation ($D = \mathrm{O}(\epsilon^3)$), when an unstable mode grows, a critical layer develops around $\omega = 0$ (*light grey region*); the width of this layer is of order ϵ in ω. Within this first critical region, a second, critical layer also develops around the special curve $y + KG_1(\Theta) = 0$. The inner critical or boundary layer is of width ϵ in θ, and has further distinguished regions near the tips of the special curve.

To continue with the critical-layer analysis we must enter a fully fledged, multi-deck, asymptotic analysis; we point out the salient features here. First, we proceed to the inner critical region and we define

$$\theta = \Delta(y, T) + \epsilon\delta \quad \text{and} \quad Z = \frac{1}{\epsilon}\zeta(\delta, y, T), \tag{58}$$

where $y + K_c G_1(\Delta, T) = 0$. Then, to leading order, we find a noisy boundary-layer solution

$$\zeta = \mathcal{N} \exp\left[\frac{1}{2D_3} K_c G_{1\theta} \left(\delta - \frac{\Delta_T}{K_c G_{1\theta}}\right)^2\right], \tag{59}$$

in the region $G_{1\theta}(\Delta, T) < 0$.

However, the inner boundary layer solution is exponentially localized and cannot be matched to the solution inside the first critical region. This is because there are slender regions at the "tips" of the special curve $y + K_c G_1 = 0$ where the scalings of the inner boundary layer break down (because $G_{1\theta} = 0$ there). For the problem at hand, these distinguished regions surround the points $(\theta, y) = (\pi/2, K_c\mathcal{G}_1)$ and $(\theta, y) = (3\pi/2, -K_c\mathcal{G}_1)$. In these "tip" regions, another expansion is needed: for example,

$$\theta = \frac{\pi}{2} + \epsilon^{2/3}\mu, \quad y = K_c\mathcal{G}_1(1 + \epsilon^{4/3}Y), \quad Z = \frac{1}{\epsilon^{2/3}}\eta(\mu, Y, T). \tag{60}$$

Fig. 18 illustrates the different regions and their scalings, and rationalizes the structure of our numerical solutions.

To leading order in each of the regions, we may then construct solutions for ρ and evaluate the contribution of each region to the integral for G. Of these, the contribution of the outer solution vanishes to leading order, and that from the tip region is higher order. Only the inner boundary layer contributes to G_1, and the resulting relation is automatically satisfied provided K_c is correctly chosen. The evolution equation for G that constitutes the ultimate goal of critical layer theory lies at higher order. Suffice to say that the analysis at this stage becomes involved and technical, but can presumably be carried through with much effort. We do not head down this tortuous route, here, and instead move onto other issues that prove more revealing.

9. Characteristics

In previous sections, we constructed asymptotic solutions in the low noise limit. The idea is that, with a small amount of noise, boundary layers can form in which the probability density saturates at finite levels. But all evidence so far suggests that the probability does not saturate when there is no noise. In this section, with $D = 0$, we present two solutions, one exact and one approximate, that illustrate the non-dissipative dynamics and bolster the conclusions we reached with numerical simulations in Section 6.

9.1. An exact solution: the case $g(\omega) = \delta(\omega)$

For a simplified special case of the Kuramoto model, we may find an exact solution using the method of characteristics. This special case is the population of coupled oscillators with identical frequencies, $g(\omega) = \delta(\omega)$, considered earlier. For such a population, only $\omega = 0$ is important, and with a symmetric initial condition, the Kuramoto system becomes

$$\rho_t - K\partial_\theta(\rho\mathcal{G}\sin\theta) = 0, \tag{61}$$

$$G(\theta, t) = -\sin\theta\int_0^{2\pi}\rho(\phi, t)\cos\phi\,\mathrm{d}\phi = -\mathcal{G}(t)\sin\theta. \tag{62}$$

The characteristic equations for this PDE are

$$\frac{\mathrm{d}\theta}{\mathrm{d}t} = -K\mathcal{G}\sin\theta \quad \text{and} \quad \frac{\mathrm{d}\rho}{\mathrm{d}t} = K\mathcal{G}\rho\cos\theta. \tag{63}$$

The solution is

$$\tan\left(\frac{\theta}{2}\right) = \tan\left(\frac{\theta_0}{2}\right)\mathrm{e}^{-Kq}, \tag{64}$$

$$\rho = \rho_0\frac{\sin\theta_0}{\sin\theta} \equiv \rho_0\frac{\mathrm{e}^{-Kq}}{\mathrm{e}^{-2Kq}\cos^2(\theta/2) + \sin^2(\theta/2)}, \tag{65}$$

where $\theta(0) = \theta_0$, $\rho(\theta_0, 0) = \rho_0(\theta_0)$, and

$$q = \int_0^t \mathcal{G}(t')\,\mathrm{d}t'. \tag{66}$$

Note that, if q becomes large, ρ must become small everywhere except over a small region of size $\theta \sim \mathrm{e}^{-Kq}$, and there $\rho \sim \mathrm{e}^{Kq} \gg 1$.

Given the solution for the probability density, $\mathcal{G}(t)$ becomes

$$\mathcal{G}(t) = \int_0^{2\pi}\rho_0\frac{\sin\theta_0}{\sin\theta}\cos\theta\,\mathrm{d}\theta. \tag{67}$$

Consider now the initial condition, $\rho_0 = (1/2\pi) + A\cos\theta_0$. Then

$$\mathcal{G}(t) = \frac{1 + 4A\pi\,\mathrm{e}^{-Kq} - \mathrm{e}^{-2Kq}}{(\mathrm{e}^{-Kq} + 1)^2}. \tag{68}$$

Finally, on recalling from the definition of q that $\mathcal{G}(t) = \mathrm{d}q/\mathrm{d}t$, we end up with the ODE

$$\frac{\mathrm{d}q}{\mathrm{d}t} = \frac{1 + 4A\pi\,\mathrm{e}^{-Kq} - \mathrm{e}^{-2Kq}}{(\mathrm{e}^{-Kq} + 1)^2}, \tag{69}$$

which can be solved in closed form.

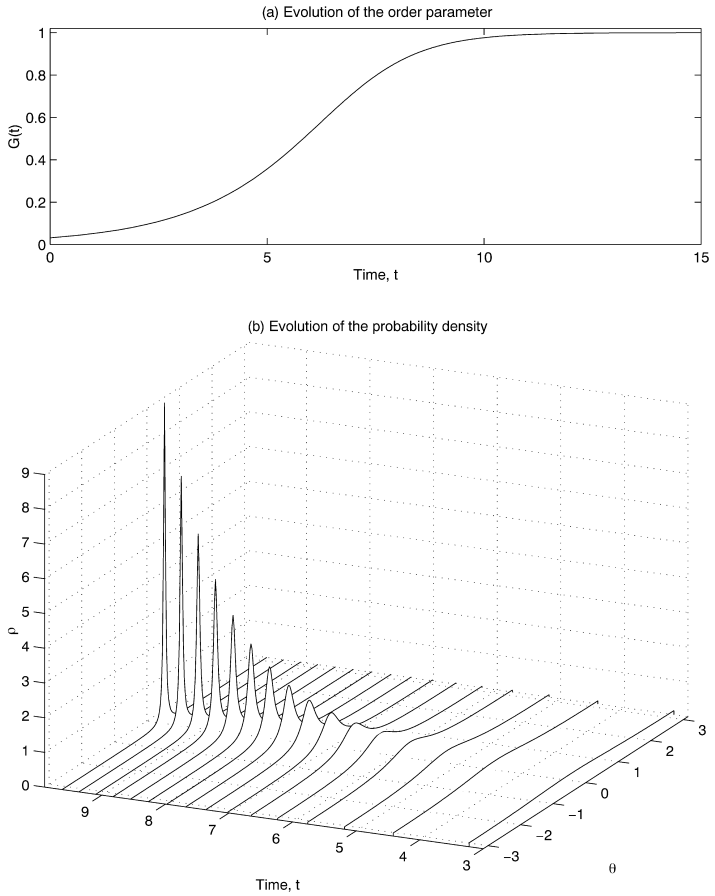

Fig. 19. Panel (a) shows the order parameter and (b) the probability density for our exact solution with $K = 1$ and $A = 0.01$.

In Fig. 19, we plot the order parameter $\mathcal{G}(t)$ and evolving probability density for $A = 0.01$. As with the numerical integrations of the system with the Lorentzian frequency distribution, the order parameter initially grows exponentially due to the linear instability (see Section 3.2), and then saturates at $\mathcal{G} = 1$.

When $\mathcal{G}$ saturates, q begins to grow linearly with time. Consequently, ρ becomes small everywhere except in a narrow region where $\theta \sim \mathrm{e}^{-Kq}$, and here the solution grows exponentially: $\rho \sim \mathrm{e}^{Kq}$. Thus, the dynamics brings probability towards a singular phase, and the solution takes the form of a spike-shaped object (or a shock-like object in the potential u, given by $u_\theta = \rho$). This is the counterpart of what we saw in the numerical simulations, though with different $g(\omega)$ and along a curve on the (θ, ω) plane. Evidently, evolution proceeds to one of the irregular solutions described in the previous section.

9.2. Populations with slowly varying order parameter

Even though we can only solve the Kuramoto model exactly in the special case described above, we may still use the method of characteristics to gain a deeper understanding of what happens in the vicinity of the synchronization threshold. In particular, for situations in which the order parameter evolves slowly, we may find approximate solutions for the limiting population density. This occurs near the threshold of linear instability, where $\mathcal{G}$ grows

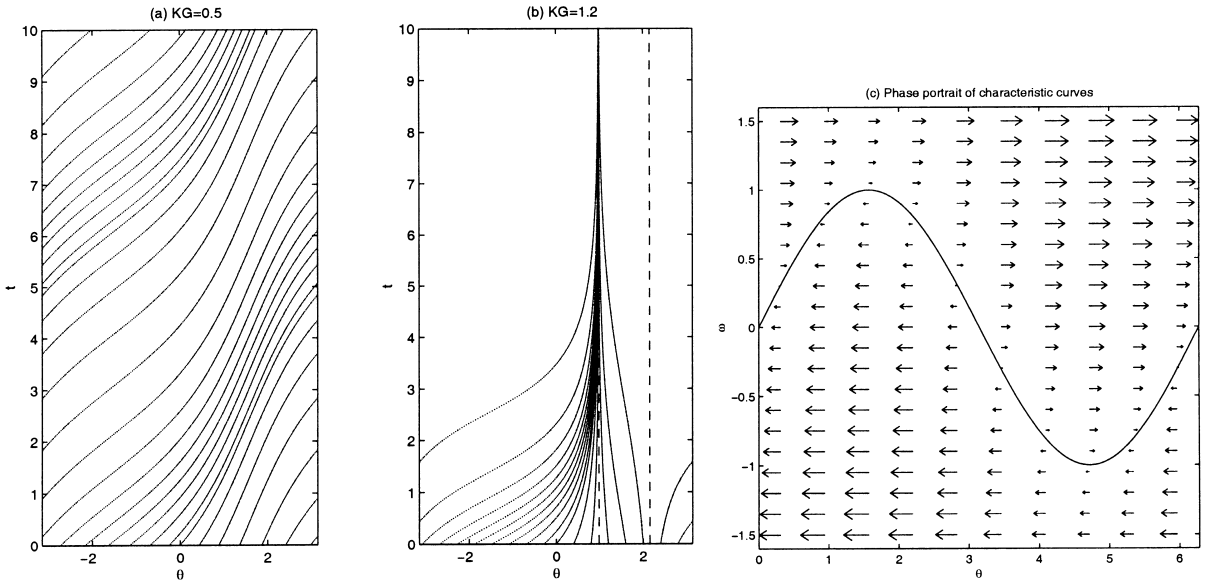

Fig. 20. Characteristic curves for (a) $\kappa = 0.5$ and (b) $\kappa = 1.2$. In (b) the vertical dashed lines show the fixed points of the equation $\dot{\theta} = \omega(1 - \kappa \sin\theta)$, of which one is stable and the other unstable. $\omega = 1$. Panel (c) shows a phase portrait of the characteristic curves on the $(\theta, \omega)-$plane for $K\mathcal{G} = 1$. The solid curve shows $\omega = K\mathcal{G}\sin\theta$.

exponentially with a small growth rate, and in the late stages of evolution of the population, where the numerical integrations of the PDE suggest that $\mathcal{G}$ saturates at a constant level.

To illustrate, we consider symmetrical systems, for which we may write the characteristic equations in the form

$$\frac{\mathrm{d}t}{1} = \frac{\mathrm{d}\theta}{\omega(1 - \kappa \sin\theta)} = -\frac{\mathrm{d}\rho}{\omega\rho\kappa\cos\theta}, \tag{70}$$

where $\kappa = K\mathcal{G}/\omega$. Hence

$$\frac{\mathrm{d}\theta}{\mathrm{d}t} = \omega(1 - \kappa \sin\theta) \quad \text{and} \quad \frac{\mathrm{d}\rho}{\mathrm{d}t} = -\omega\rho\kappa\cos\theta. \tag{71}$$

The complication in solving this system lies in the time dependence of κ. But if $\kappa \approx$ constant, we find

$$\tan(\theta/2) = \begin{cases} \kappa + \sqrt{1-\kappa^2}\tan\pi\psi & \text{if } \kappa^2 < 1, \\ \kappa - \sqrt{\kappa^2-1}\tanh\pi\phi & \text{if } \kappa^2 > 1, \end{cases} \tag{72}$$

$$\rho(1 - \kappa \sin\theta) = \text{constant}, \tag{73}$$

where $\psi = \omega(t - t_0)\sqrt{1-\kappa^2}/2\pi$ and $\phi = \omega(t - t_0)\sqrt{\kappa^2-1}/2\pi$ and t_0 is a constant.

Depending on whether κ^2 is greater or less than unity, the characteristic curve either continually winds in angle ($\kappa^2 < 1$), or converges to the point $\theta = \Delta = \sin^{-1}(1/\kappa)$ ($\kappa^2 > 1$); see Fig. 20. In the $\kappa^2 < 1$ region, (73) indicates that ρ oscillates in time. Where $\kappa^2 > 1$, however, $\rho = \text{constant}/(1-\kappa\sin\theta)$ focusses continually into the vicinity of the special angle, $\theta = \Delta$; the convergence of the characteristics is our analogy with shock formation. The focussing is illustrated further in Fig. 21, which reproduces many of the features of the full numerical solution.

The characteristic curves of the PDE also have significance for the discrete Kuramoto model. For large N, one is tempted to take the ODE (1) and replace the sum by an integral (see [4,6]). For symmetrical systems, the resulting

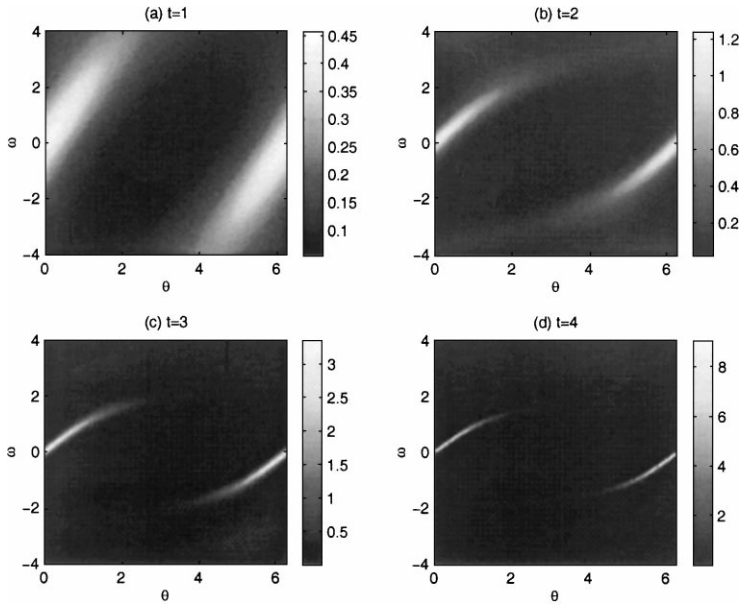

Fig. 21. The evolving probability density predicted by solution (73) with $K\mathcal{G} = 1$.

ODE is exactly the θ-equation solved above. In other words, the characteristic curves are the orbits of the oscillators in the continuum limit, and so the phase portrait in Fig. 20 shows the evolution of individual oscillators for constant $\mathcal{G}$.

10. Discrete vs. continuous

The discussion of characteristics ultimately leads us back to the discrete version of Kuramoto's model, and in this section we undertake a more systematic comparison of the finite dimensional system with the solutions of the PDE. The underlying question we address in this section is whether the continuous approximation, made in the limit $N \to \infty$, predicts the dynamics of a finite number of oscillators. That is, if the results obtained in the previous sections are applicable to Eq. (1).

10.1. Synchronized structures in phase space

To compare the PDE solutions with the discrete model, one can prepare the results of the simulation of the ODEs in the same way as Figs. 4 and 10 (i.e., counting the instantaneous population density in sub-intervals of phase and frequency). Figs. 22 and 23 show the pictures that result on replotting the data also shown Fig. 1. These should be compared with Figs. 4 and 10. The initial behaviours of the continuous and discrete models are much the same: we see the probability gathering into tilting stripes on the (θ, ω)-plane. Furthermore, for the unstable case, the probability continues to build up in the vicinity of the special curve (compare Figs. 23 and 10).

10.2. Finite sampling and drifts

Despite some similarities between the PDE and ODEs, there are important differences. For example, one peculiarity of the unstable discrete case is that the concentration of probability drifts in θ (see Figs. 1 and 23). This

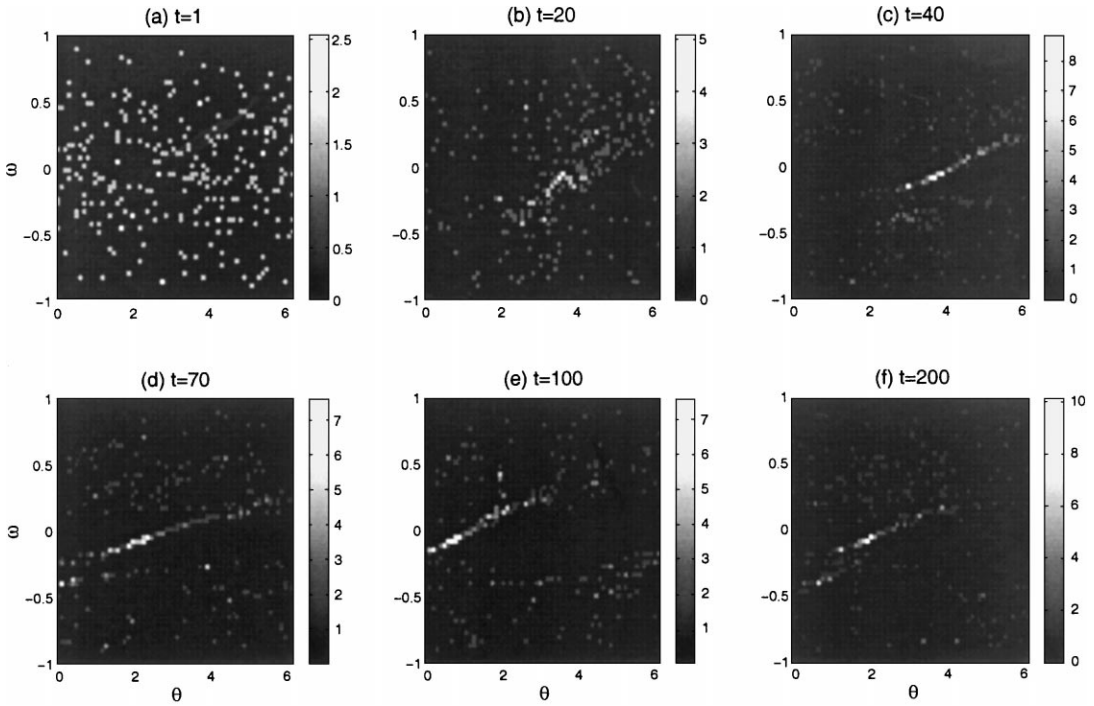

Fig. 22. The discrete probability density at six successive instants from the numerical integration of Kuramoto's ODEs. This is a sub-threshold population and corresponds to Fig. 1a (see caption of Fig. 1 for more details of the computation). The θ and ω axes are sub-divided into 64 intervals and the density is obtained by counting the number of oscillators in each bin.

is primarily related to the fact that, although the frequency distribution from which the intrinsic frequencies are extracted is symmetric, any finite sampling of the actual population is biased to either positive or negative frequencies. This induces an asymmetry in the population that can lead to a drift. If we prepare a discrete population in which the initial frequencies are chosen in pairs with opposite signs, so that the frequency distribution is artificially *symmetrized*, then the drift largely disappears, as shown in Fig. 24.

10.3. Residual synchronization and ephemeral structures

Another feature of the discrete model is that at sub-threshold coupling strengths, although the order parameter remains at low levels, $r(t)$ does not decay (see Fig. 1). Moreover, in Figs. 1a and 22, coherent structures are evident. These structures drift irregularly and resemble the formations that appear above the critical threshold. In some cases, they persist indefinitely; in others, they occasionally disappear and reform, often at different phases.

In any finite population, one expects fluctuations in $r(t)$, and standard arguments suggest that these should scale as $1/\sqrt{N}$. Indeed, the low-level fluctuations in the order parameter show precisely this scaling with N; see Fig. 25 and also [24]. But the detailed time evolution of the fluctuations also seems intimately connected to the ephemeral coherent structures. Moreover, there are strong periodicities in the order parameter that are not associated with any important intrinsic variability of the uncoupled oscillators (in Fig. 1, there is an obvious strong periodicity with a frequency $\omega \approx 0.3$).

Some rationalization for the sub-threshold structures comes from the nonlinear effects observed in the numerical simulations of the PDE. There we saw that nonlinearity acts to focus probability into narrow regions to create sharp

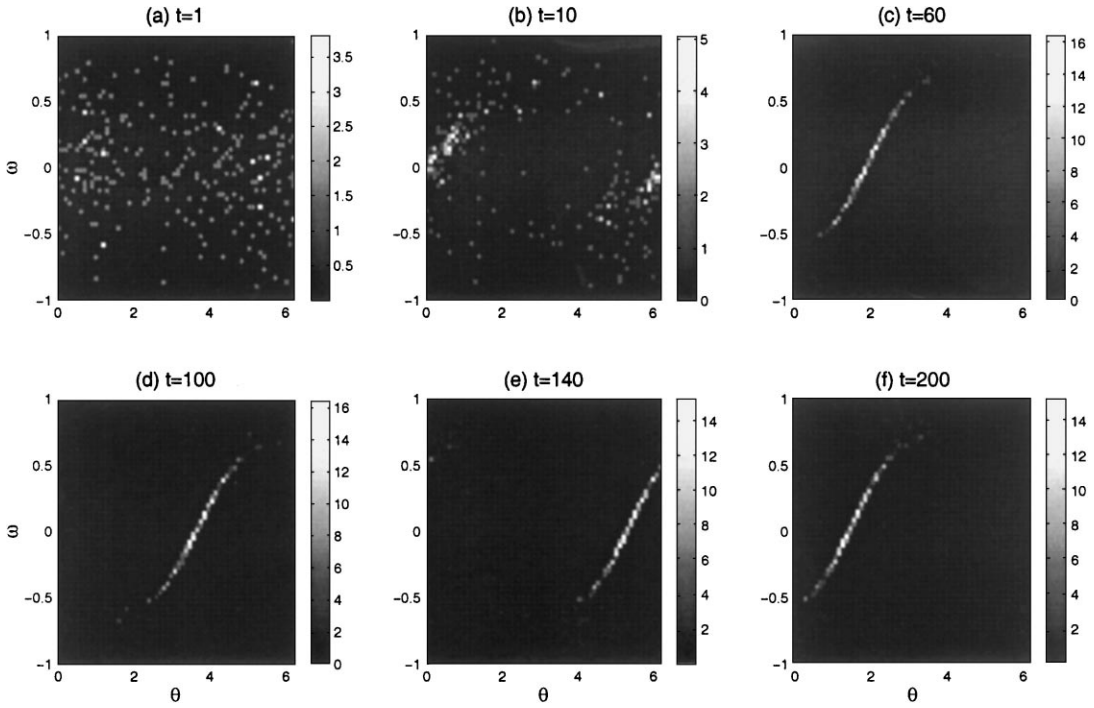

Fig. 23. The discrete probability density at six successive instants from the numerical integration of Kuramoto's ODEs. This is a super-threshold population, corresponds to Fig. 1b (see caption of Fig. 1 for more details of the computation), and is constructed in the same way as Fig. 22.

peaks in probability even for $K < K_c$. However, in the continumm model, these regions subsequently tilt over and phase mix, leading to the leading to the decay of the order parameter. By contrast, in the discrete model, the order parameter remains at low amplitude, and the probability concentrations sustain themselves against tilting.

10.4. Finite-sampling curiosities

In addition to asymmetries that can induce drift in phase, the finite sampling of the frequency distribution can also have some other unusual effects. For example, some samplings can lead to sustained synchronization in the population for $K < K_c$. Conversely, other samples are essentially incoherent even if $K > K_c$.

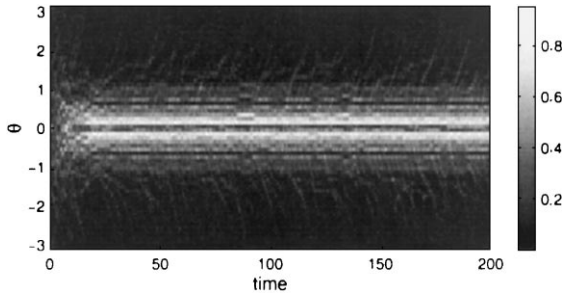

Fig. 24. Evolution of the phase distribution for a realization of the discrete model with $D = 0.01$, $K = 0.8$ and $N = 256$. The initial conditions in this case are *symmetrized* by selecting $\pm$ pairs of frequencies, and the synchronized cluster does not drift. $\xi = 0.01$, $a = 2$ and $L = 0$.

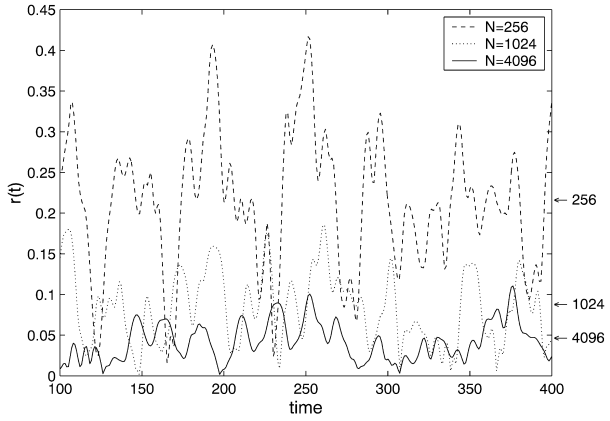

Fig. 25. Order parameters for the discrete model with $N = 256$, 1024 and 4096, for $D = 0$, $K = 0.65$ and the standard initial conditions with $\xi = 0.1$, $a = 2$ and $L = 0$. The arrows indicate the mean values in the three cases, which decay like $N^{-1/2}$.

A different kind of "curiosity" is shown in Fig. 26, which shows an example in which the initial sampling is symmetrized (as described above) and produces a population with a bi-modal frequency distribution. Such distributions can suffer oscillatory instabilities [10,25], and the evolution shown in Fig. 26 is certainly more reminiscent of an oscillating population than a convergence to steady synchronized cluster. Panel (b) of this figure shows the discrete analogue of the mean field amplitude:

$$\mathcal{G}_D(t) = \frac{1}{N}\sum_{j=1}^{N} \cos\theta_j. \tag{74}$$

Another example is displayed in Fig. 27. For this population, there is an irregular switching on a long timescale between a partially synchronized state in which the probability density is concentrated near $\theta = 2n\pi$, and a

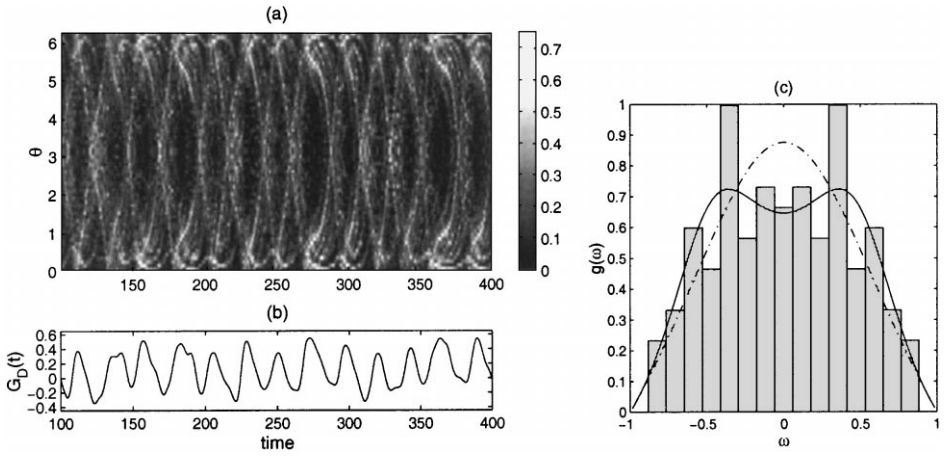

Fig. 26. Evolution of (a) the phase distribution and (b) the amplitude of the mean field, $\mathcal{G}_D(t)$, for an anomalous realization of the discrete model with $N = 256$, $K = 0.8$ and $D = 0$. The realization is anomalous because the actual sampling of the frequency distribution, shown in panel (c), produces a bimodal population which suffers an oscillatory instability. $\xi = 0.1$, $a = 2$ and $L = 0$. In (c), the dot-dashed curve shows distribution (24), and the solid curve shows a fitted bi-modal distribution.

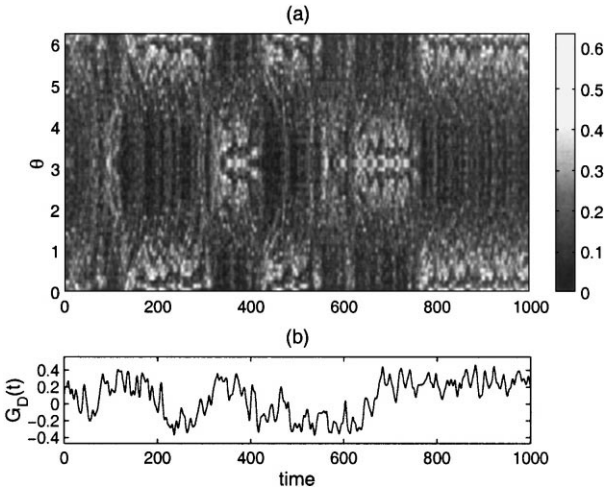

Fig. 27. Evolution of (a) the phase distribution and (b) the amplitude of the mean field, $\mathcal{G}_D$, for an anomalous case in which there is an irregular switching on long timescales between states with probability concentrations at $\theta = 2n\pi$ and states with concentrations at $\theta = (2n+1)\pi$, $n = 0, 1, 2, \ldots$. $K = 0.8$, $D = 0$, $\xi = 0.1$, $a = 2$ and $L = 0$.

similar state with concentrations around $\theta = (2n+1)\pi$, $n = 0, 1, \ldots$. Simultaneously, the mean field amplitude, $\mathcal{G}_D(t)$, shows reversals of sign. This sequence occurs on a relatively long timescale and reminds one of a low-order dynamical system with perturbed heteroclinic orbits. In fact, such orbits are expected near the Takens–Bogdanov bifurcation (in which a complex pair of eigenvalues bifurcate to instability with zero frequency), which are known to occur for populations with bi-modal frequency distribution [25]. Thus, finite sampling can lead to phenomena more usually associated with populations with more complicated frequency distributions.

11. Conclusions

In this study, we have explored the transition to synchronization in a population of weakly coupled oscillators governed by the continuum limit of Kuramoto's model. What we have seen is that, when the coupling strength exceeds some noise-dependent threshold, the population develops spike-like solutions with noisy boundary layers (for $D \neq 0$), or into a delta function (when $D = 0$). This behaviour parallels what happens in the discrete version of the Kuramoto model.

However, the discrete model also has other features not captured by the PDE if the population is finite. For example, we have seen that much more complicated behaviour can occur for sub-threshold coupling strengths. Here, the finite population has complicated temporal dynamics and behaviour (ephemeral coherent structures, switching patterns) which reminds one of the spatio-temporal complexity seen in the complex Ginzburg–Landau and Kuramoto–Sivashinsky equations. Certainly, this dynamics deserves more investigation.

The onset of synchronization in the Kuramoto model is quite unlike what happens in nearly inviscid shear flows and almost ideal plasmas, despite similarities in the linear stability problem. There, a global instability "overturns" the equilibrium structure in a thin critical layer, leading to the formation of a cat's eye pattern. In the characteristic curves, this pattern corresponds to an array of elliptic islands and hyperbolic points connected by separatrices, much like the phase portrait of the pendulum. For the Kuramoto model, the instability develops in very different way, and the structure of the characteristic curves is rather different. Moreover, we have also seen that the sub-threshold

dynamics of the coupled oscillators is unlike that of the plasma or fluid. Thus not all bifurcations of modes from a continuous spectrum are governed by similar dynamics. This raises the question of what details of the problem are important to determining the dynamics of the instability, and poses the problem of catagorizing the different kinds of bifurcations. Certainly, we have ignored one important aspect of the fluid and plasma systems: both have an underlying Hamiltonian structure of a similar flavour. Curiously, and by contrast, in another recent model of a coupled oscillator population [26] (with a built-in Hamiltonian structure) the bifurcation to instability is identical to the plasma and fluid problem.

Lastly, it has been suggested [3,4] that the Kuramoto model is very special in the form of its mean-field interaction. More specifically, the coupling has the form, $N^{-1}K\sum_n f(\theta_n-\theta_m)$ with $f(\phi)=\sin\phi$. With this coupling, a characteristic scaling of the order parameter emerges in the vicinity of the critical coupling strength: $r\sim(K-K_c)^\alpha$ with $\alpha=\frac{1}{2}$. Yet, Daido and Crawford and Davies suggest that couplings with $f(\theta)$ a generic function, produce ordered states that do not scale in this way. In fact, $\alpha=1$ is the typical case.

Daido's analysis is based on a generalization of Kuramoto's theory, and considers steadily oscillating, noise-free populations; effectively, it generalizes the contents of Section 7.4. Daido contends with arbitrary coupling functions and intrinsic frequency distributions; his theory becomes mathematically complicated as a result. Crawford and Davies present a theory based on an extension of the centre-manifold method. They are able to extract systematically the scaling α, but the result of the theory is an amplitude equation for the unstable mode containing an infinite number of terms. Neither Daido nor Crawford and Davies offer an intuitive physical explanation of why $\alpha=1$ is the generic scaling and Kuramoto's scaling is special.

To explore this issue further we have performed some additional studies with the coupling function, $f(\theta)=\sin\theta+\sigma\sin 2\theta$. A key feature of this modified coupling term is that it neither changes the linear stability theory of the $m=1$ mode, nor breaks the symmetry, $\rho(\theta,\omega,t)=\rho(-\theta,-\omega,t)$ (the origin of the generic scaling has nothing to do with the existence of this symmetry). The latter allows us to write

$$G(\theta,t)=-\mathcal{G}_1(t)\sin\theta-\mathcal{G}_2(t)\sin 2\theta, \tag{75}$$

where

$$\mathcal{G}_m(t)=\sigma^{m-1}\int_{-\infty}^{\infty}\int_0^{2\pi}\rho(\theta,\omega,t)g(\omega)\cos m\theta\,\mathrm{d}\theta\,\mathrm{d}\omega,\quad m=1,2 \tag{76}$$

are a pair of new mean-field components, with corresponding order parameters, $r_m=|\mathcal{G}_m|$.

The modification to the coupling function does not change any of the arguments surrounding the structure of slightly noisy steady populations or the characteristic curves of the PDE: one still expects the steady populations to divide into noisy synchronized boundary layers and a de-synchronized outer population, and the characteristic curves to trace out orbits that converge to a section of the curve defined by $\omega+KG=0$. Thus, although the geometry of the synchronizing zone will be slightly modified, the overall aspect of the solutions should not be very different. Indeed, this is precisely what one observes in simulations of the discrete model [4], and in Fig. 28, which shows numerical solutions of the PDE with $\sigma=-\frac{1}{2}$; the appearance of the solution is little different from the "special" Kuramoto case.

Despite the apparent similarity of the structure of the solution, the scaling of G implies that the extent of the synchronizing zone is much smaller in the generic case than for Kuramoto's example (see also Fig. 28). To understand why this is so, we have explored the numerical solutions in detail and derived a version of Daido's theory in the special case at hand. We conclude that the scaling is determined by the way that the oscillator population contributes to the mean field. More specifically, Daido's theory implies that, just beyond onset and for steady noise-free solutions, we may divide the integrals in (76) into contributions from the synchronizing zone and from the de-synchronized

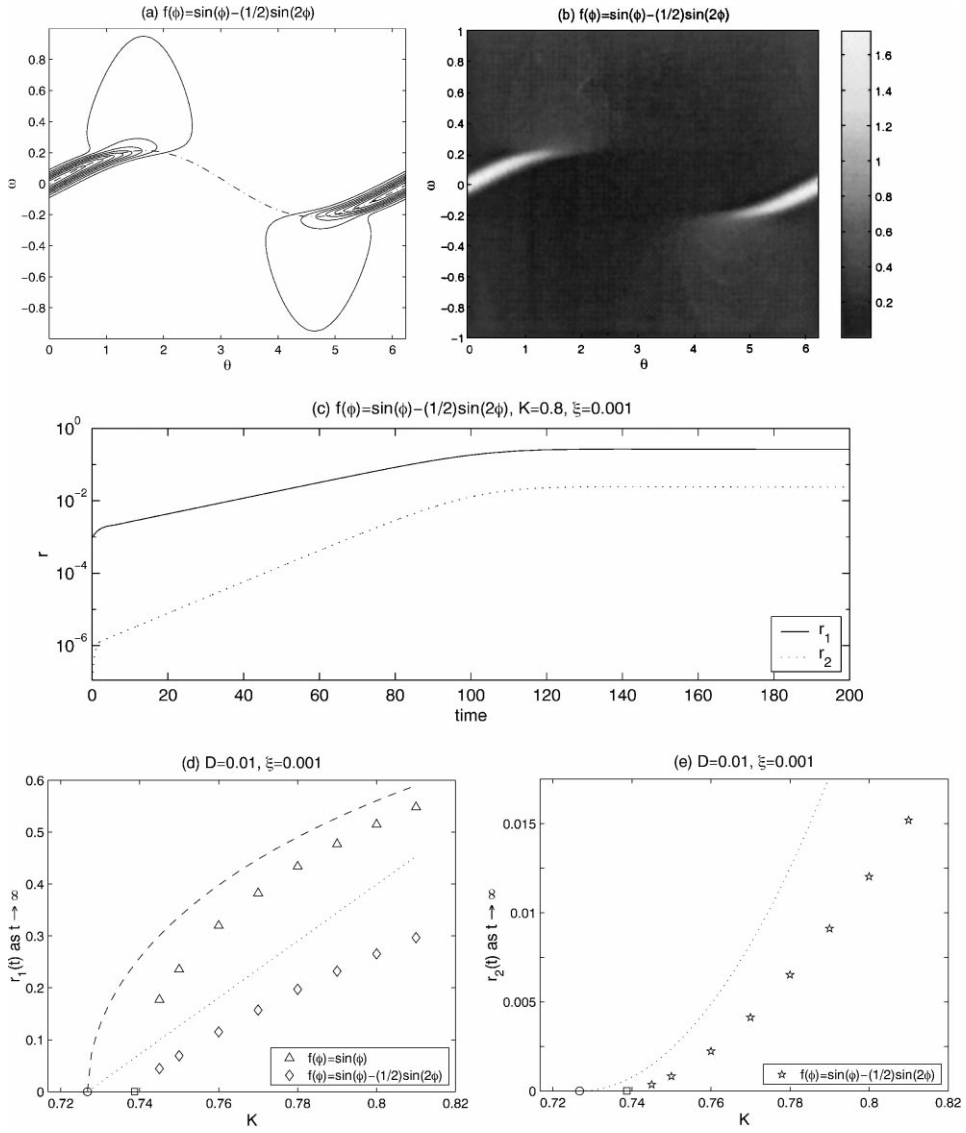

Fig. 28. Panels (a) and (b) show $\rho(\theta,\omega,t)$ at $t=200$ obtained from a numerical integration with $K=0.8$, $a=2$, $L=0$ and $\xi=0.001$. The coupling function is $f(\phi)=\sin\phi-\frac{1}{2}\sin 2\phi$ (so $\sigma=-\frac{1}{2}$). In panel (a), we superimpose the line, $\omega=K\mathcal{G}_1\sin\theta-\frac{1}{2}K\mathcal{G}_2\sin 2\theta$, on a contour plot of ρ, where $\mathcal{G}_1$ and $\mathcal{G}_2$ are set to the final, steady values obtained in the integration. The time histories of the order parameters are shown in panel (c). In panels (d) and (e) we show the final value (at $t=200$ or more) of the order parameters r_1 and r_2 as functions of K. In panel (d), we also display the same result for Kuramoto's coupling ($\sigma=0$). The circles show the critical coupling for $D=0$ ($K_c=2-4/\pi$) and the square in (d) shows K_c for $D=0.01$ ($K_c=0.739$). The dotted lines show the expected values of r_1 for $D=0$ according to the current version of Daido's theory: for the compact frequency distribution, $r_1\approx 3\pi^4(K-K_c)/[8(\pi-2)^2(\pi+2)]$ and $r_2\approx(\pi^2-4)\mathcal{G}_1^2/(4\pi^2)$. The dashed line shows the asymptotic theory for Kuramoto's case.

oscillators outside it. Further approximations in the vicinity of onset then indicate that, for the Lorentzian frequency distribution (and assuming $\mathcal{G}_1$ positive),

$$\mathcal{G}_1=\tfrac{1}{2}K\mathcal{G}_1+\frac{16}{3\pi}\mathcal{G}_2+\mathrm{O}((K-K_c)^3)\quad\text{and}\quad\mathcal{G}_2=\sigma(2\mathcal{G}_2+\mathcal{G}_1^2)+\mathrm{O}((K-K_c)^3),\tag{77}$$

which imply that

$$r_1 = \frac{3\pi|1-2\sigma|}{32|\sigma|}(K-K_c) + O((K-K_c)^2) \quad \text{and} \quad r_2 = \frac{9\pi^2|1-2\sigma|}{1028|\sigma|}(K-K_c)^2 + O((K-K_c)^3). \quad (78)$$

The key feature of these formulae that is elementally different from Kuramoto's case is the presence of the $\mathcal{G}_1^2$ contribution to $\mathcal{G}_2$. These are *outer-field* contributions from the desynchronized oscillators. In other words, the onset of the synchronization through $m = 1$ induces a nonlinear mean field in the desynchronized part of the population that organizes an $m = 2$ response (measured by $\mathcal{G}_2$). This, in turn, reacts back on the synchronizing population to limit its growth. The overall effect is a saturating, quadratic nonlinearity. For Kuramoto's model, the outer field *never* contributes to the mean field and the saturation of the instability occurs through a cubic nonlinearity coming from the synchronizing zone (see Section 7). (This term is also present for the modified coupling, but lies at higher order.) The nonlinear effects can also be observed in the numerical solutions. For example, Fig. 28 shows the scaling of $\mathcal{G}_1$ and $\mathcal{G}_2$ with $K - K_c$, which is in agreement with the asymptotic theory. (The computations are slightly dissipative, and this shifts the onset of synchronization and modifies the solution branch.)

The quadratic saturation effect is quite different to what happens for a dissipative population. There, the controlling nonlinearity is always cubic, which results from the rotational symmetry of the incoherent equilibrium and demands that the amplitude equation be invariant with respect to changing the sign of $a(T)$, the amplitude of the unstable mode. For the noise-free system, this symmetry effect no longer operates because the creation of a singular distribution in ρ (the synchronized oscillators) immediately breaks the symmetry and allows quadratic nonlinearity to feed back on the growing mode. In other words, the convergence to the irregular distribution breaks the Hopf scaling.

Acknowledgements

This work was initiated and partly conducted at the 1999 Geophysical Fluid Dynamics Summer Study Program, Woods Hole Oceanographic Institution, which is supported by the National Science Foundation and the Office of Naval Research. We are grateful to many of the participants for comments and conversations. We also appreciate conversations with A. Bernoff and P. Smereka. RS was supported by the Isabella Bonadonna 1998 fellowship from the Associazione Elettronica ed Elettrotecnica Italiana. NJB acknowledges an equipment grant from the Nuffield Foundation.

References

[1] A.T. Winfree, Biological rhythms and the behaviour of populations of coupled oscillators, J. Theor. Biol. 16 (1967) 15.
[2] Y. Kuramoto, in: H. Araki (Ed.), Proceedings of the International Symposium on Mathematical Problems in Theoretical Physics, Lecture Notes in Physics, Vol. 39, Springer, New York, 1975, pp. 420–422.
[3] J.D. Crawford, T.R. Davies, Synchronization of globally coupled phase oscillators: singularities and scaling for general couplings, Physica D 125 (1999) 1.
[4] H. Daido, Onset of cooperative entrainment in limit-cycle oscillators with uniform all-to-all interactions: bifurcation of the order function, Physica D 91 (1996) 24.
[5] K. Wiesenfeld, P. Colet, S.H. Strogatz, Synchronization transitions in a disordered Josephson series array, Phys. Rev. Lett. 76 (1996) 404.
[6] Y. Kuramoto, Chemical Oscillations, Waves and Turbulence, Springer, New York, 1984.
[7] H. Sakaguchi, Cooperative phenomena in coupled oscillator systems under external fields, Prog. Theor. Phys. 79 (1987) 39.
[8] S.H. Strogatz, R.E. Mirollo, Stability of incoherence of a population of coupled oscillators, J. Stat. Phys. 63 (1991) 613.
[9] L.L. Bonilla, J.C. Neu, R. Spigler, Nonlinear stability of incoherence and collective synchronization in a population of coupled oscillators, J. Stat. Phys. 67 (1992) 313.
[10] J.D. Crawford, Amplitude expansions for instabilities in populations of globally-coupled oscillators, J. Stat. Phys. 74 (1994) 1047.

[11] J.D. Crawford, Amplitude equations for electrostatic waves: universal behaviour in the limit of weak instability, Phys. Plasmas 2 (1995) 97.
[12] D. del Castillo-Negrete, Nonlinear evolution of perturbations in marginally stable plasmas, Phys. Lett. 241 (1998) 99.
[13] K. Stewartson, Marginally stable inviscid flows with critical layers, IMA J. Appl. Math. 27 (1981) 133.
[14] S.M. Churilov, I.G. Shukhman, The nonlinear development of distrurbances in a zonal shear flow, Geophys. Astrophys. Fluid Dynamics 38 (1987) 145.
[15] M.E. Goldstein, S.J. Leib, Nonlinear roll-up of externally excited free shear layers, J. Fluid Mech. 191 (1988) 481.
[16] N.J. Balmforth, Shear instability in shallow water, J. Fluid Mech. 387 (1999) 97.
[17] S.H. Strogatz, R.E. Mirollo, P.C. Matthews, Coupled nonlinear oscillators below the synchronization threshold: relaxation by generalized Landau damping, Phys. Rev. Lett. 68 (1992) 2730.
[18] H. Weitzner, Plasma oscillations and Landau damping, Phys. Fluids 6 (1963) 1123.
[19] N.J. Balmforth, D. del Castillo Negrete, W.R. Young, Dynamics of vorticity defects in shear, J. Fluid Mech. 333 (1997) 197.
[20] M.R. Feix, P. Bertrand, A. Ghizzo, in: B. Perthame (Ed.), Advances in Kinetic Theory and Computing, World Scientific, Singapore, 1994, pp. 45–81.
[21] G. Manfredi, Long-time behaviour of nonlinear Landau damping, Phys. Rev. Lett. 79 (1997) 2815.
[22] N.J. Balmforth, S.G. Llewellyn Smith, W.R. Young, Disturbing vortices, J. Fluid Mech., accepted for publication.
[23] B.F. Farrell, The initial growth of disturbances in a baroclinic flow, J. Atmospheric Sci. 39 (1982) 1663.
[24] H. Daido, J. Stat. Phys. 60 (1990) 753.
[25] L.L. Bonilla, C.J.P. Vicente, R. Spigler, Time-periodic phases in populations of nonlinearly coupled oscillators with bimodal frequency distributions, Physica D 113 (1998) 79.
[26] P. Smereka, Synchronization and relaxation for a class of globally coupled Hamiltonian systems, Physica D 124 (1998) 104.